An observational study of tropical-cyclone spin-up in Supertyphoon Jangmi (2008) from 24 - 27 September

N. T. Sanger[1], M. T. Montgomery[2,], R. K. Smith[3], and M. M. Bell[2]

[1]{United States Air Force Weather, Barksdale Air Force Base, Louisiana}

[2]{Department of Meteorology, Naval Postgraduate School, Monterey, California}

[3]{Department of Physics, University of Munich, Munich, Germany}

Correspondence to: N. T. Sanger (nlsanger@gmail.com)

Abstract

An observational study of tropical-cyclone intensification is performed using dropsondes, in situ flight-level data, satellite imagery, and ELDORA radar during the spin-up of Tropical Storm Jangmi (2008) in the Western North Pacific. This event was observed with research aircraft during the Tropical Cyclone Structure 2008 (TCS08) field experiment over the course of three days as Jangmi intensified rapidly from a tropical storm to a supertyphoon. The dropsonde analysis indicates that the peak azimuthally-averaged storm-relative tangential wind speed occurs persistently within the boundary layer throughout the spin-up period and suggests that significant supergradient winds are present near and just within the radius of maximum tangential winds. An examination of the ELDORA data in Tropical Storm Jangmi reveals multiple rotating updrafts near the eye beneath low cloud top temperatures $\leq$ -65°C. In particular, there is a 12 km-wide, upright updraft with a peak velocity of 9 m s^{-1} with co-located strong low-level ($z < 2$ km) convergence of 2×10^{-3} s^{-1} and intense relative vorticity of 4×10^{-3} s^{-1}. The analysis of the corresponding infrared satellite imagery suggests that rotating updrafts are omnipresent before and during rapid intensification.

The findings of this study support a new paradigm of tropical-cyclone intensification in which rotating deep convective cells are prevalent during tropical-cyclone spin-up and in which the maximum tangential wind occurs within the vortex boundary layer where supergradient winds occur near and within the radius of maximum tangential winds.

Report Documentation Page

Form Approved
OMB No. 0704-0188

1. REPORT DATE	2. REPORT TYPE	3. DATES COVERED
2012		**00-00-2012 to 00-00-2012**

4. TITLE AND SUBTITLE	5a. CONTRACT NUMBER
An observational study of tropical-cyclone spin-up in Supertyphoon Jangmi (2008) from 24 - 27 September	5b. GRANT NUMBER
	5c. PROGRAM ELEMENT NUMBER
6. AUTHOR(S)	5d. PROJECT NUMBER
	5e. TASK NUMBER
	5f. WORK UNIT NUMBER
7. PERFORMING ORGANIZATION NAME(S) AND ADDRESS(ES) **Naval Postgraduate School,Department of Meteorology,Monterey,CA,93943**	8. PERFORMING ORGANIZATION REPORT NUMBER
9. SPONSORING/MONITORING AGENCY NAME(S) AND ADDRESS(ES)	10. SPONSOR/MONITOR'S ACRONYM(S)
	11. SPONSOR/MONITOR'S REPORT NUMBER(S)

12. DISTRIBUTION/AVAILABILITY STATEMENT
Approved for public release; distribution unlimited

13. SUPPLEMENTARY NOTES
Atmos. Chem. Phys., submitted : 2012

14. ABSTRACT

An observational study of tropical-cyclone intensification is performed using dropsondes, in situ flight-level data, satellite imagery, and ELDORA radar during the spin-up of Tropical Storm Jangmi (2008) in the Western North Pacific. This event was observed with research aircraft during the Tropical Cyclone Structure 2008 (TCS08) field experiment over the course of three days as Jangmi intensified rapidly from a tropical storm to a supertyphoon. The dropsonde analysis indicates that the peak azimuthally-averaged storm-relative tangential wind speed occurs persistently within the boundary layer throughout the spin-up period and suggests that significant supergradient winds are present near and just within the radius of maximum tangential winds. An examination of the ELDORA data in Tropical Storm Jangmi reveals multiple rotating updrafts near the eye beneath low cloud top temperatures ≤ -65?C. In particular, there is a 12 km-wide, upright updraft with a peak velocity of 9 m s-1 with co-located strong low-level (z < 2 km) convergence of 2 ?10-3 s-1 and intense relative vorticity of 4 ?10-3 s-1. The analysis of the corresponding infrared satellite imagery suggests that rotating updrafts are omnipresent before and during rapid intensification. The findings of this study support a new paradigm of tropical-cyclone intensification in which rotating deep convective cells are prevalent during tropical-cyclone spin-up and in which the maximum tangential wind occurs within the vortex boundary layer where supergradient winds occur near and within the radius of maximum tangential winds.

15. SUBJECT TERMS

16. SECURITY CLASSIFICATION OF:			17. LIMITATION OF ABSTRACT	18. NUMBER OF PAGES	19a. NAME OF RESPONSIBLE PERSON
a. REPORT	b. ABSTRACT	c. THIS PAGE			
unclassified	**unclassified**	**unclassified**	**Same as Report (SAR)**	**49**	

1 Introduction

While a 45% (3% yr^{-1}) decrease in the 48-h track forecast error of tropical cyclones has been achieved between 1990 and 2005, only a modest decline of approximately 17% (1.1% yr^{-1}) in the 48-h intensity forecast errors has been attained over the same period (Rogers et al. 2006). The lack of improvement in intensity forecasting may be due in part to a lack of complete knowledge of the physics and dynamics of spin-up. In addition, there is no consensus on the dominant tropical-cyclone intensification mechanism.

Recent work has suggested the importance of the boundary layer and its role in the intensification process. However, a lack of observations of boundary-layer structure during intensifying storms limits our ability to evaluate this work.

To provide a context for this observational study, we review briefly three major spin-up paradigms that have been proposed over the past fifty years. The classical, or 'conventional' view of tropical-cyclone spin-up features a deep layer of convectively-induced convergence of absolute angular momentum, *M*, above the boundary layer, where the flow is assumed to be approximately frictionless so that *M* is materially conserved (Charney and Eliassen 1964, Ooyama 1969, Carrier 1971, Willoughby 1990). A second paradigm developed over the past two and half decades emphasizes thermodynamic processes and focuses in particular on a postulated positive feedback loop involving the near-surface wind speed and the evaporation of water from the underlying ocean, with the evaporation rate being a function of wind speed and thermodynamic disequilibrium (Emanuel 1989, 1995, 1997, 2003; see also Holton 2004). A third and recent paradigm highlights the role of rotating deep convection[1] and their vorticity remnants in organizing the vorticity structure of the core, but as in previous theories, these clouds collectively drive the spin-up of the system-scale vortex by producing radial inflow above the boundary layer. As in the earlier paradigms, radial convergence of *M* above the boundary layer in conjunction with its material conservation leads to spin-up of the bulk tangential winds and an increasing radial pressure gradient there. In contrast, this new paradigm stresses the fact that the spin-up of the maximum tangential winds actually occurs in the boundary layer. At low levels, *M* is reduced by the frictional torque, but the radial inflow

[1]The term "rotating deep convection" is used in lieu of vortical hot towers (VHTs), which were first described in Hendricks et al. (2004) and later studied in Montgomery et al. (2006a) and Nguyen et al. (2008), among others. To avoid any potential controversy that surrounds the definition of VHTs, the term 'rotating deep convection' will be used throughout the rest of this paper. Usage of the term VHT has led some to the impression that only extremely intense convection has strong rotation. However, a recent study by Wissmeier and Smith (2011) suggests that all rotating deep convection should be considered in total, since they showed that even moderate convection can have a greater impact on stretching of low-level relative vorticity than the most intense convection. Thus, a broad definition is required for studying the aggregate impact of these convective elements on tropical cyclone spin-up.

is much stronger than above. Spin-up occurs there when the radial inflow is large enough to converge rings of air to small radii faster than the rate at which M can be removed by friction. The increase of the tangential wind by this mechanism naturally leads to the development of supergradient flow and an accompanying outward agradient force. The agradient force acts to decelerate the radial inflow at the base of the eyewall, whereupon air parcels turn upwards and carry their elevated tangential momentum into the eyewall. This process contributes also to the spin-up of the tangential winds in the bulk vortex (Smith et al. 2009; Bui et al. 2009; Smith and Thomsen 2010; Smith and Montgomery 2010).

The strong low-level radial inflow in the inner-core region has been documented in individual cases by Montgomery et al. (2006b), Bell and Montgomery (2008), Bell et al. (2012), and by Zhang et al. (2011) in a recent composite of dropsonde observations in mature and intensifying tropical cyclones. While these studies offer support for elements of the foregoing paradigm, they fall short of demonstrating the chain of processes for the boundary-layer spin-up mechanism articulated above.

Two complementary field experiments conducted in the summer of 2008 in the Western North Pacific used research aircraft to collect data in tropical disturbances and intensifying tropical storms. For details on these field campaigns, the reader is referred to Parsons et al. (2008) and Elsberry and Harr (2008). During the experiments, two typhoons, Jangmi and Nuri, were documented in considerable detail over a period of several days as they intensified, offering an opportunity to investigate the role of the boundary layer in spin-up. In addition, data obtained using the ELDORA radar acquired during the tropical storm stage of Jangmi provide an opportunity to document the presence of rotating deep convection during intensification. The present paper presents the results of such an investigation for Supertyphoon Jangmi.

The paper is organized as follows. Section 2 includes a brief description of Jangmi's history. Section 3 discusses data collection and the analysis methodology used. In section 4, we examine the intensification of Jangmi over a three-day period and carry out an azimuthally-averaged analysis to determine the height of the peak tangential wind. We use this analysis also to quantify the departure of gradient wind balance in the inner-core boundary-layer region of the developing vortex. Section 5 presents analyses of the ELDORA radar observations during the spin-up of Tropical Storm (TS) Jangmi in conjunction with high-

resolution satellite imagery. Finally, Section 6 presents a summary and conclusions drawn from the results.

2 Storm history

Supertyphoon Jangmi developed from a westward-propagating disturbance that crossed over the Western North Pacific Ocean near longitude 170°E on 17 September 2008. After struggling to develop for nearly a week, the storm organized quickly and was declared a tropical depression at 1200 UTC 23 September, when it was located approximately 435 km south-southwest of Guam (Chu et al. 2009). The tropical depression evolved rapidly into a tropical storm just 12 hours later at 0000 UTC 24 September as it moved on a primarily northwestward track along the periphery of the low to mid-level subtropical ridge to its northeast. The Joint Typhoon Warning Center (JTWC) best-track is shown in Figure 1.

Jangmi continued to intensify steadily with upper-level divergence over its center and strong poleward outflow inferred from the satellite imagery (not shown). During the third penetration of the storm by the WC-130J aircraft at 2359 UTC 24 September, the radar imagery (not shown) indicated that the eye diameter decreased from around 111 km to 59 km in just over 2 h (Sanger 2008a). Six hours later, at 0600 UTC 25 September, the storm was declared a typhoon with 1-min average sustained surface wind speeds of 33 m s^{-1} and a minimum central pressure of 974 hPa (Chu et al. 2009). Over the next 18 hours, Jangmi began the first of its two rapid-intensification (15 m s^{-1} increase in surface wind speed within 24-h period) phases and reached an intensity of 46 m s^{-1} by 0000 UTC 26 September, which is shown in the JTWC best-track intensity (Figure 2).

Subsequently, Jangmi experienced a second rapid intensification phase and was declared a supertyphoon at 0000 UTC 27 September with an intensity of 69 m s^{-1}. A United States Air Force Reserve (USAFR) WC-130J reconnaissance aircraft flying at approximately 3 km above the ocean surface measured maximum flight-level winds of 84 m s^{-1} at 0616 UTC 27 September. In addition, a dropsonde near the center of the storm indicated a surface pressure of 905 hPa at 0924 UTC and a peak surface wind speed of 71 m s^{-1} at 0751 UTC (Sanger 2008b). According to the JTWC best-track data, Supertyphoon Jangmi reached its peak intensity of 72 m s^{-1} at 0600 UTC 27 September approximately 790 km southeast of Taipei, Taiwan.

3 Data and analysis methodology

Together, the USAFR WC-130J and a Naval Research Laboratory (NRL) P-3 flew a total of six research missions in Jangmi from the tropical depression to the supertyphoon stage (Figure 2). The NRL P-3 aircraft collected high-resolution ELDORA data in the storm while it was a weak tropical depression, a tropical storm, and a mature Category 5 tropical cyclone. Since this research is focused on inner-core tropical-cyclone spin-up, we will discuss primarily the in situ and ELDORA data collected during intensification from the tropical storm stage.

3.1 In situ flight-level data

The USAFR 53rd Weather Reconnaissance Squadron (i.e., "Hurricane Hunters") aircrews provided the High-Density/High-Accuracy (HD/HA) flight-level data that includes geopotential height, extrapolated sea-level pressure (SLP), air temperature, dew-point temperature, wind direction, wind speed, and the peak 10-s average surface wind speed from the Stepped Frequency Microwave Radiometer (SFMR). The High-Density Observation (HDOB) message transmits 30-s averages of the HD/HA data from the WC-130J aircraft, with the exception of the peak value data mentioned above (Williamson 2009, Ch. 5). For more information on the SFMR data, the reader is referred to Uhlhorn et al. (2007).

The NRL P-3 1-s flight-level data were provided by NCAR/Earth Observing Laboratory (EOL).

3.2 GPS dropsondes

The primary observational tool used in this study is the NCAR Global Positioning System (GPS) dropwindsonde (hereafter dropsonde or sonde) produced by Väisälä. The GPS dropsonde measures pressure, temperature, relative humidity (PTH), and horizontal wind speed at 2 Hz temporal resolution (0.5 s^{-1}) along a Lagrangian trajectory while descending at a rate between 12 m s^{-1} and 15 m s^{-1} in the lower troposphere. The fall speed of the dropsonde results in a vertical resolution of around 5 m. The average PTH errors are less than 1.0 hPa, 0.2°C, and 5% respectively, and wind errors are less than 0.5 m s^{-1}. The reader is referred to Hock and Franklin (1999) and Franklin et al. (2003) for more information on the GPS dropsonde.

Quality control of the entire set of dropsondes was performed by the National Center for Atmospheric Research/Earth Observing Laboratory (NCAR/EOL). In addition, a manual investigation of each sounding was made to eliminate any bad data points that were missed by the quality control software.

3.3 Storm center determination

To investigate the inner-core structure of Jangmi, we converted the in situ data from Cartesian to cylindrical coordinates in a storm-relative reference frame. Accurate center estimates to within 5 km are required for an appropriate coordinate transformation.

The WC-130J aircraft center fixes were used to create a storm track file. The JTWC best-track centers were used to ensure a reasonable starting point for the cubic spline interpolation to the first aircraft center fix. The storm centers and storm motion data were fit using a cubic spline interpolation method, and then linearly interpolated to a 10-min storm track file. Using a simple linear interpolation, this track file was then used to determine the storm-relative position and storm-relative wind for each observation point along the flight track and dropsonde descent.

The aircraft center fixes have an estimated accuracy to within one-half of the diameter of light and variable winds in the center (Williamson 2009, pp. 5–11). The mean accuracy of the centers for the tropical storm, typhoon, and supertyphoon during the individual missions were approximately 7 km, 5 km, and 3 km, respectively. Thus, the storm centers for TS Jangmi may not have been accurate enough for an appropriate transformation into storm-relative coordinates. To ensure the inherent center errors did not significantly affect the results, a sensitivity analysis of the errors on the radial and tangential winds was carried out (see Sanger 2011, Chapter 3, Section E). The results of the analysis indicated mean RMSE values of ~ 2 m s^{-1} for both the radial and tangential wind speeds obtained from the dropsonde data with storm center errors less than or equal to 5 km.

To mitigate any significant errors in the analysis of TS Jangmi due to inaccurate center fixes (> 5 km), we used the Willoughby and Chelmow (1982) storm centers that were made available by the National Oceanographic and Atmospheric Administration/Hurricane Research Division (NOAA/HRD). These fixes, which typically have an accuracy to within ~ 3 km, were used to create a storm track file as detailed above.

3.4 Compositing technique

A simple compositing technique using bins based on storm-relative dropsonde location was used to develop the azimuthal-mean of various kinematic and thermodynamical variables. The kinematic quantities of storm-relative tangential and radial velocities were calculated. In addition, the thermodynamical variables of potential temperature (θ) and virtual potential temperature (θ_v) were computed. The dropsonde data were linearly interpolated to a 50 m vertical grid from the surface to an altitude of 2000 m above the surface. The vertical grid was created using an interpolation function in the Interactive Data Language (IDL) computer program to fill in for missing data in the compositing. However, the program did not extrapolate beyond where the data record ends.

3.5 Gradient wind

Dropsonde observations and HDOB flight-level data were used to obtain an estimate of the azimuthally-averaged pressure gradient for the calculation of the gradient wind curves during Jangmi's spin-up. The gradient wind curve was computed from the radial pressure gradient per unit mass derived from the dropsonde data using the gradient wind equation from Holton (2004, p. 61). The gradient wind curve was placed on a radial plot for comparison with the tangential wind speed measured by the dropsondes. The reader is referred to Sanger (2011, Ch.3, Section G) for details.

3.6 Satellite and ELDORA radar data

High-resolution infrared, visible, and microwave satellite imagery were used to determine the extent and temperature of cloud tops. They were used also to provide a quantitative assessment of the characteristics of updrafts in Jangmi to complement the results of the ELDORA mesoscale analyses of cells underneath low cloud-top temperatures ($\leq$ -65°C).

The NRL P-3 ELDORA data collected on 24 September were analyzed during the tropical storm stage of Jangmi to diagnose the structure of relative vorticity, convergence, and vertical velocity underneath convective cells with low cloud-top temperatures and to determine if rotation was present in the lower troposphere as suggested in modeling studies. The reader is referred to Hildebrand et al. (1995, their Figure 2) and Testud et al. (1995) for more detailed information on the ELDORA radar.

4 An azimuthally-averaged view of Jangmi's spin-up

The three-day evolution of the azimuthally-averaged, inner-core structure of Jangmi in the radial and vertical plane is examined utilizing in situ high-density flight-level observations and 39 eye and eyewall dropsondes released during all three stages of the storm. The dropsondes were deployed from a USAFR WC-130J flying at an altitude of approximately 3 km and a NRL P-3 flying at around 3.5 km altitude. The dropsonde paths and multiple aircraft radial penetrations into Jangmi as a tropical storm, typhoon, and supertyphoon are shown in Figures 3a, 4a, and 5a. The radial and vertical coverage of the dropsonde data points are shown in Figures 3b, 4b, and 5b. Microwave satellite imagery in Figures 3c, 4c, and 5c is shown to provide the context of storm structure for each of the three stages.

4.1 Characteristics of the low-level wind field

The near-surface locations of the Jangmi eyewall dropsondes are shown in Figures 6a,c,e and the storm-relative tangential wind speeds for all three stages of the storm are displayed in Figures 6b,d,f. The altitudes of the plotted tangential winds are at the estimated height of the maximum tangential wind speed in the eyewall on each day.

The evolution of the tangential wind speed shown in Figures 6b,d,f reveals that the RMW becomes much more distinct, and closer to the storm center. Based on Figures 6d,f, the RMW is estimated to be 55 km for Typhoon Jangmi and 24 km for Supertyphoon Jangmi. Due to the asymmetric wind field and the small number of observations in TS Jangmi, we use the HDOB SFMR wind data to obtain a more accurate estimate of the RMW at both flight level and the surface.

The SFMR total wind observations and flight level winds retrieved from the HDOB 30-s data were used to estimate the RMW in each quadrant of TS Jangmi (see Table 1). A cubic polynomial curve was fit to all of the data points to estimate the axisymmetric mean RMW (Sanger 2011, Figure 16). The RMW average at flight level was ~100 km and the SFMR RMW was ~75 km.

4.2 Individual eyewall dropsondes

Since the kinematic composites of the eyewall region shown later in Figure 12 are based on 28 dropsondes, it is of interest to study the individual dropsondes released in the eyewall (Figures 7 - 9). A majority of the radial wind profiles of these sondes during the evolution of

Jangmi show a radial inflow layer from the surface to between 600 m and 1000 m altitude. The peak tangential wind speed in 26 of the 28 sondes occurred *within* the boundary layer, whose depth was estimated to be at least 1250 m – 1500 m based on the layer of gradient wind imbalance discussed below in Section 4.5 and shown later in Figure 13. Furthermore, 23 of the 28 sondes had the maximum tangential wind speed at or below an altitude of 600 m. Several profiles had peak tangential winds between 100 m and 300 m above the sea surface.

4.3 Kinematic composites

The azimuthal composites of tangential and radial wind for all three stages of Jangmi are shown in Figure 10 for the eye (center of circulation out to a radius at which the tangential wind remains $\leq$ 10 m s^{-1}), eyewall (region with deep convection and tangential winds at least 80 percent of the RMW value), outer core (twice the RMW out to the radius of gales), and ambient (just beyond outer core to ~ 800 km radius) regions of the storm. In all three stages, there is mean radial inflow from the surface to an altitude of at least 1 km. The peak azimuthally-averaged tangential wind speeds are observed at an altitude of around 500 m in TS Jangmi and Supertyphoon Jangmi and about 650 m in Typhoon Jangmi. It will be shown later in Figure 13 that these altitudes are well within the azimuthal-mean boundary layer of the system-scale circulation. These results agree well with the observational results of (Franklin et al. 2003; Powell et al. 2003; Montgomery et al. 2006b; Bell and Montgomery 2008; Giammanco et al. 2008), the theoretical studies of Kepert (2001), Zhang et al. 2001, and Smith et al. (2009), and the numerical-model results of Kepert and Wang (2001), which found also that the maximum wind speeds occurred at a height of around 500 m. The new intensification paradigm of Smith et al. (2009) discussed in Section 1, provides a dynamical explanation for how the maximum tangential winds could exist in the frictional boundary layer, which leads to the development of supergradient winds in this region.

4.4 Gradient wind

Figures 11a,c,e show the cubic polynomial curve fits to the pressure data from the HDOB and dropsonde observations. The curve fits are judged to be very good with coefficient of determination values (r^2) between 0.92 and 0.98 (Figures 11a,c,e) The dashed blue curves in Figures 11b,d,f are the gradient wind estimates derived from the cubic polynomial fit to the dropsonde pressure data. On all three days, the tangential winds are most supergradient near and just within the RMW relative to the dropsonde-derived gradient wind curve. The dashed

green curves in Figures 11b,d,f are an independent estimate of the axisymmetric gradient wind using the HDOB data, when they are available. Both calculations indicate the presence of supergradient winds near the RMW during the spin-up of the storm[2].

The significantly increased scatter of the pressure data and the reduced r^2 values found in Figure 11a raises a question about the representativeness of the axisymmetric gradient wind during the tropical storm stage of Jangmi due to the large degree of convective asymmetry apparent in satellite (Figure 3c) and radar observations (not shown). The cubic polynomial curve fit and radial profiles in individual quadrants of the HDOB-extrapolated sea-level pressure, geopotential height, and tangential wind (Sanger 2011, Figure 17, Figures 50-52) reveal asymmetries in these fields also.

To investigate the issue of asymmetries in TS Jangmi described above, we used the HDOB data to perform an uncertainty estimate of the gradient wind. The uncertainty estimate was conducted via a quadrant-by-quadrant analysis using the more frequent 30-s HDOB extrapolated sea-level pressure data. Although the HDOB data also has limitations in the eyewall region (assumptions of a constant radial pressure gradient from flight level to the surface and hydrostatic balance in a region of significant upward and downward vertical velocities), it was determined that these data were reasonable to use as a proxy of the axisymmetric pressure field for the TS stage only, since these limitations of assuming a constant radial pressure gradient and hydrostatic balance were found to be minimal (Sanger 2011, Ch. 4, Section 2c).

The error estimate was computed using the steepest pressure-gradient curve (NE Quadrant) and the flattest pressure-gradient curve (WSW Quadrant) to compute an estimated upper and lower bound of the gradient wind curve. In this estimate, it was assumed that the radius of curvature of the tangential wind (i.e., primary circulation) was equal to the local radius. These two curves provide a reasonable uncertainty estimate of the asymmetric pressure field observed in TS Jangmi. The upper and lower-bounding curves of the gradient wind are plotted with the HDOB and dropsonde-derived gradient wind curves and is shown in Figure 12.

In Figure 12, the gradient wind associated with the steepest pressure gradient curve (NE Quadrant-solid orange line) still lies below five supergradient wind observations near and just

[2] (Sanger 2011, Appendix C-E) shows similar results at the five other altitudes analyzed.

within the RMW. Note also that the dropsonde curve is very similar to the gradient wind curve obtained using the flattest pressure gradient (WSW Quadrant-dotted purple line). The difference between the upper and lower bound gradient wind curves is approximately 5 m s^{-1} just outside the RMW and then around 6 - 7 m s^{-1} near and just within the RMW. This difference is used to define an uncertainty estimate of ~ $\pm$ 3 m s^{-1} for the gradient wind curve.

From Figure 12 we see also that the tangential wind speeds are in excess of the mean HDOB-derived gradient wind curve (dashed green line) by 5 - 6 m s^{-1}. The tangential winds still exceed the largest HDOB-derived gradient wind speed curve by at least 1 m s^{-1} after considering the estimated $\pm$ 3 m s^{-1} error in the gradient wind curve and 2 m s^{-1} RMSE for the tangential wind due to the center uncertainty.

The quadrant-by-quadrant gradient wind analysis at 500 m altitude derived from the extrapolated sea-level pressure for each of the six radial legs shown in Sanger (2011, Figures 49b,d,f,h,j,l) shows at least one observation of supergradient winds in each quadrant (ESE-1; WSW-1; SSE-1; NE-1; NW-1; SE-2). Moreover, all seven of the supergradient observations in each quadrant lie above the $\pm$ 3 m s^{-1} error bar estimated in the foregoing paragraph[3].

4.5 Boundary layer

As discussed in Smith and Montgomery (2010) there is a plethora of definitions of the boundary layer. In their analyses of numerical simulations, Smith et al. (2009) chose to use the depth of strong inflow (radial wind speeds exceeding 2 m s^{-1}), which is reasonably well defined in their calculations. However, since the boundary layer owes its existence to the inward agradient force brought about by the reduction of the tangential wind component by surface friction, an alternative definition would be to take the depth of significant gradient wind imbalance, for example, the height at which the tangential wind equals 90% of the gradient wind. We refer to this as the dynamical definition of the boundary layer. Some authors have used a thermodynamic definition of the boundary layer to characterize the depth of the mixed layer based on the virtual potential temperature structure. Since mixing in the hurricane boundary layer is primarily associated with shear-generated turbulence we consider this definition to have little dynamical significance. However, since the data are available we show the depth of this layer for comparison.

[3] For details of the error analysis, the reader is referred to Sanger (2011, Ch. 4, Section 3d).

Figure 13 shows the composite wind and thermal structure of the boundary layer during the evolution of Jangmi. In the figure, VT and VR denote the tangential and radial components of storm-relative wind, respectively, VPOT denotes the virtual potential temperature, and PT denotes the potential temperature. The depth of the significant low-level radial inflow (VR ≥ 20% of its near-surface value) is shown with the solid black horizontal line labeled "Inflow." The height of the peak tangential wind speed is depicted with a solid black horizontal line labeled "VT MAX." The estimated dynamic boundary-layer depth is denoted by the solid black horizontal line labeled "GWB." The thermodynamic boundary-layer depth is depicted by the solid black horizontal line labeled "TD."

These data indicate that the dynamical boundary layer is much deeper than the well-mixed layer, consistent with the findings of Zhang et al. (2009) and Zhang et al. (2011). Of particular significance, on all three days the average maximum tangential wind component lies well within the dynamical boundary layer and within the layer of significant radial inflow.

5 An asymmetric view of Jangmi's spin-up

5.1 Background

Recent studies by Montgomery et al. (2006a) and Wissmeier and Smith (2011) have noted that stretching vertical vorticity by growing convection increases the ambient rotation by more than one order of magnitude and that the vorticity remains for a long time after the initial updraft has decayed. The predicted vorticity levels are comparable with those observed in recent research on tropical depressions (Houze et al. 2009; Bell and Montgomery 2010; Raymond and Carillo-Lopez 2011). One of the main findings in Wissmeier and Smith (2011) was that even moderately deep convection could lead to a larger amplification of the ambient vorticity than the deep convection. Thus, one should focus not only on the extremely deep convection, but consider also the less intense convection in the aggregate.

Deep convective cells of varying intensity were observed during the spin-up of Jangmi. A brief investigation of this convective activity is presented first to provide a context for a quantitative assessment of the vorticity and convergence in some of the updrafts in TS Jangmi using results from the ELDORA mesoscale analysis of cells that were underneath low cloud-top temperatures of ≤ -65°C.

5.2 Analysis of deep convection

The evolution of convective cells during the spin-up of Jangmi is shown using satellite imagery in Figures 14 and 15 during the tropical storm stage. Between 2030 UTC 24 September and 0257 UTC 25 September, two major convective bursts commenced at 2030 UTC 24 September (Panels 1-7 in Figure 14 and Panels 1-5 in Figure 15) and 2330 UTC 24 September (Panels 8-12 in Figure 14 and Panels 6-12 in Figure 15). These bursts consisted of the development of cells and their associated anvil clouds near the center of TS Jangmi with extremely low cloud-top temperatures of $<$ -85°C. Throughout this period, the anvil clouds grew in areal coverage and merged into one large cloud region of extremely cold cloud tops covering a horizontal area of around 46,000 km^2. This sequence of events was observed throughout the rest of Jangmi's spin-up into a supertyphoon (not shown). Additional information about the nature of convection during Jangmi's spin-up is provided by a timely CLOUDSAT pass at 1709 UTC 25 September, which sampled a cell in the storm's southern quadrant located near the center of the storm and extending to an altitude of nearly 17 km (Figure 16).

5.3 ELDORA radar observations in Tropical Storm Jangmi

The ELDORA radar onboard the NRL P-3 observed some of the deep convection in TS Jangmi on 24 September 2008. There were many instances where the radar sampled enhanced levels of vertical vorticity within convective clouds. As an illustration, we show an example of a convective complex with a well-defined vertical vorticity signature. Here, the ELDORA domain for the period 2310 – 2320 UTC 24 September is overlaid with the MTSAT infrared imagery on 2313 UTC 24 September, which shows extremely low cloud-top temperatures of $<$ -75°C (Figure 17). The motivation for this radar analysis is to determine whether the convection located underneath the cold infrared imagery cloud tops of TS Jangmi during 2310 – 2320 UTC 24 September has rotation.

The analysis of the 1.5 km altitude radar data displayed in Figure 18a reveals convection arrayed in spiral bands around the storm center. Earth-relative winds in Figure 18b indicate strong southerly to southeasterly flow of 35 m s^{-1} to 40 m s^{-1} located in the outermost spiral band. The innermost spiral band has lower wind speeds between 12 m s^{-1} and 27 m s^{-1}. The vertical vorticity and vertical velocity in Figure 18c reveal three regions of co-located positive relative vorticity and vertical updrafts that are associated with convective cells in the southern

portion of the ELDORA domain. In this region, large relative vorticity on the order of 2×10^{-3} s^{-1} and vertical velocities between 4 m s^{-1} and 5 m s^{-1} are analyzed. Both of these regions are also in areas of significant low-level convergence on the order of 2×10^{-3} s^{-1} (Figure 18d). A few other areas of enhanced relative vorticity, convergence, and vertical velocity with values of 2×10^{-3} s^{-1}, 2×10^{-3} s^{-1}, and 2 m s^{-1}, respectively, are found in the northern half of the outer spiral band.

In the outermost spiral band in Figures 18c,d, there are multiple updraft and downdraft dipoles, as well as positive and negative relative vorticity dipoles. The most dominate dipole pattern is observed in the lower right portion of Figure 18c,d. In contrast, the innermost spiral band contains primarily couplets of updrafts and positive relative vorticity.

The analysis of the 8.0 km altitude ELDORA radar data in Figure 19a reveals reflectivity values between 18 dBZ to around 30 dBZ at and south of y = 20 km and between x = 63 km and x = 75 km. Earth-relative winds in Figure 19b indicate southerly to southeasterly flow of 21 m s^{-1} - 27 m s^{-1} in the outermost spiral band. The innermost spiral band contains lower wind speeds between 2 m s^{-1} and 15 m s^{-1}. Near the center of the outermost spiral band, enhanced vertical vorticity values of 2×10^{-3} s^{-1} are co-located with strong updraft vertical velocities of over 9 m s^{-1} and divergence of approximately 3×10^{-3} s^{-1} (Figures 19c,d). There is also a smaller region of elevated levels of co-located positive relative vorticity on the order of 1×10^{-3} s^{-1} and upward vertical velocities of 1 – 3 m s^{-1}.

The ELDORA radar analysis at both 1.5 km and 8.0 km altitude shows that underneath this region of extremely cold infrared cloud tops there are multiple rotating deep convective cells. To investigate this further, a vertical cross-section of the strongest updraft is taken at y = 20 km (denoted by the dashed red line in Figures 18a and 19a).

The vertical cross-section in Figure 20a reveals the existence of strong, upright radar reflectivities greater than 45 dBZs that extend to an altitude of around 6 km with a horizontal extent of about 12 km and echo tops stretching up to an altitude of more than 15 km. Strong updraft velocities on the order of 4 m s^{-1} - 9 m s^{-1} are analyzed in the moderate to strong radar reflectivities rising to around 11 km altitude.

In Figure 20c, an area of strong vertical vorticity is co-located with a 12 km wide vertical updraft from an altitude of 1.5 km up to 13 km. Two intense relative vorticity peaks of greater than 4×10^{-3} s^{-1} at heights of 3 km and 11 km are co-located with ~ 3 – 4 m s^{-1}

vertical velocities. There is a maximum vertical velocity of 9 m s^{-1} in between the two vertical vorticity peaks, at an altitude of 8 km that is co-located with vertical relative vorticity of approximately 0.5×10^{-3} s^{-1}. Large horizontal convergence values between 2×10^{-3} s^{-1} and 3.5×10^{-3} s^{-1} are analyzed below 2 km altitude and between 4 km and 6 km altitude.

The findings here are consistent with those obtained in previous studies of convective-scale asymmetric features of tropical cyclones using airborne Doppler radar and dropsonde data (Marks and Houze 1984; Reasor et al. 2005; Reasor et al. 2009; Houze et al. 2009; Bell and Montgomery 2010; Raymond and Carrillo-Lopez 2011). The observed occurrence of vortical deep convection is consistent also with recent numerical modeling studies of Hendricks et al. (2004), Montgomery et al. (2006a), Nguyen et al (2008), Shin and Smith (2008), and Fang and Zhang (2011), which suggested the importance of vortical convection to spin-up.

6 Summary and conclusions

An observational study of the spin-up of Supertyphoon Jangmi was carried out using data collected during the TCS-08 field experiment. These data include GPS dropsondes, ELDORA radar, and satellite imagery. Individual and composite vertical profiles of the dropsonde data were examined to determine the structure of the inner-core boundary layer of the intensifying storm. It was shown that the composite-mean maximum tangential wind speed lies well within the boundary layer on all three days.

An estimate of the departure of gradient wind balance was obtained at selected heights up to 1500 m from the dropsonde data. The analyses suggest the presence of significant supergradient winds within the boundary layer and near the RMW in all three stages of the storm evolution. The largest supergradient winds occurred near and just inside the RMW during peak intensity. The evidence suggesting the existence and spatial structure of supergradient winds near and within the RMW supports the argument advanced in Smith et al. (2008), Smith et al. (2009), and Smith and Montgomery (2010) that unbalanced boundary-layer dynamics in the inner-core region are an important component in the determination of the maximum axisymmetric mean radial and tangential flow at all times during the evolution of the storm.

Fluid dynamical reasoning suggests deep convection in a rotating environment should be vortical in nature. This expectation is confirmed by the ELDORA radar analysis, which showed multiple areas of vortical deep convection in the inner-core circulation some hours

before its intensification to a typhoon. In one instance, there was a region of large cyclonic vorticity on the order of 2×10^{-3} s^{-1} co-located with a 12 km wide, vertical updraft, which contained average velocities of around 4 – 5 m s^{-1} and a peak of 9 m s^{-1} at 8 km altitude. This region also had strong low-level convergence. This feature was co-located with a region of low cloud top temperatures as observed in the satellite imagery.

These findings are consistent with those obtained in previous studies of convective-scale asymmetric features of tropical cyclones using airborne Doppler radar. On the basis of the results presented here, we suggest that rotating deep convection, and the accompanying system-scale spin-up mechanisms described in the introduction, were the primary spin-up pathway for Tropical Cyclone Jangmi. The ELDORA analysis reveals multiple regions of cyclonically rotating updrafts during the tropical storm stage of development. The dropsonde analyses offer plausible evidence also in support of the new theory that the maximum azimuthal mean tangential wind speed occurs within the boundary layer and axisymmetric supergradient winds exist in the boundary layer, near and just within the RMW of an intensifying tropical cyclone. Further study of multiple storms using ELDORA radar to diagnose rotating deep convective cells for longer periods of time during spin-up is required to adequately assess the impacts of these structures on the primary circulation.

The results presented here are consistent with the new intensification paradigm discussed in the Introduction. We acknowledge that this is only one storm and clearly, further studies of this type are called for in other storms to assess the generality of these findings. In view of the caveats involved with the axisymmetric gradient wind calculations in this study, future work should aim to release dropsondes more frequently across the RMW during each radial leg to allow improved resolution of the radial pressure gradient there and permit an assessment of whether supergradient winds exist in the boundary layer at the tropical storm stage more generally. As a first step in this direction, such an analysis is being conducted for the spin-up portion of Tropical Storm Earl, which rapidly intensified to a major hurricane during a recent 2010 field experiment. The results of this analysis will be reported in due course.

Acknowledgements

We are grateful to NPS, the Office of Naval Research (Grant #N001408WR20129) and the National Science Foundation for sponsoring the TCS08/TPARC field experiment and

supporting our participation in the experiment and our analysis of the data. We would like to thank Peter Black at the Naval Research Laboratory in Monterey and Russ Elsberry, Frank Giraldo, and Pat Harr at Naval Postgraduate School for their helpful comments. We also express our gratitude to NOAA/HRD for providing the Willoughby and Chelmow (1982) derived storm centers for Jangmi. We extend our appreciation to NCAR/EOL for providing the quality controlled dropsonde and NRL P3 flight-level data for analysis. Lastly, we would like to offer our sincere thanks to the brave NRL P3 and WC-130J "Hurricane Hunter" aircrews that courageously flew into these tropical tempests to collect data so that we may better understand the spin-up process.

References

Bell, M. M., and Montgomery, M. T.: Observed structure, evolution, and potential intensity of Category 5 Hurricane Isabel (2003) from 12 to 14 September, Mon. Wea. Rev., 136, 2023–2046, 2008.

Bell, M. M. and Montgomery, M. T.: Sheared deep vortical convection in pre-depression Hagupit during TCS08, Geophys. Res. Lett., 37, L06802, doi:10.1029/2009GL042313, 2010.

Bell, M. M., Montgomery, M. T., and Lee, W.-C.: An axisymmetric view of concentric eyewall evolution in Hurricane Rita (2005), J. Atmos. Sci., in press, 2012.

Bui, H. H., Smith, R. K., Montgomery, M. T., and Peng, J.: Balanced and unbalanced aspects of tropical cyclone intensification, Q. J. R. Meteorol. Soc., 135, 1715–1731, 2009.

Carrier, G. F.: The intensification of hurricanes. J. Fluid Mech., 49, 145-158, 1971.

Charney, J. G. and Eliassen, A.: On the growth of the Hurricane Depression, J. Atmos. Sci., 21, 68-75, 1964.

Chu, J. H., Levine, A., Daida, S., Schiber, D., Fukada, E., and Sampson, C. R.: JTWC Western North Pacific best-track data, http://www.usno.navy.mil/NOOC/nmfc-ph/RSS/jtwc/best_tracks/2008/2008s-bwp/bwp192008.txt, 2009.

Cooper, G. A. and Falvey, R. J.: 2008 Annual tropical cyclone report, U.S. Naval Maritime Forecast Center/Joint Typhoon Warning Center Pearl Harbor, Hawaii, 117 pp., 2009.

Elsberry, R. L. and Harr, P. A.: Tropical cyclone structure (TCS08) field experiment: Science basis, observational platforms, and strategy, Asia-Pacific J. Atmos. Sci., 44, 209–231, 2008.

Emanuel, K. A.: The finite-amplitude nature of tropical cyclogenesis, J. Atmos. Sci., 46, 3431–3456, 1989.

Emanuel, K. A.: Sensitivity of tropical cyclones to surface exchange coefficients and a revised steady-state model incorporating eye dynamics, J. Atmos. Sci., 52, 3969–3976, 1995.

Emanuel, K. A.: Some aspects of hurricane inner-core dynamics and energetics, J. Atmos. Sci., 54, 1014–1026, 1997.

Emanuel, K. A: Tropical Cyclones, Annu. Rev. Earth Planet, Sci., 31, 75-104, doi:10.1146/annurev.earth.31.100901.141259, 2003.

Fang, J. and Zhang, F.: Evolution of multiscale vortices in the development of Hurricane Dolly (2008), J. Atmos. Sci., 68, 103-122, 2011.

Franklin, J. L., Black, M. L., and Valde, K.: GPS dropwindsonde wind profiles in hurricanes and their operational implications, Wea. Forecasting, 18, 32–44, 2003.

Giammanco, I. M., Schroeder, J. L, Powell, M. D., and Smith, D. A.: GPS dropwindsonde observations of tropical cyclone low-level wind maxima, Extended Abstracts, 28th Conf. on Hurricanes and Tropical Meteorology, Orlando, FL, Amer. Meteor. Soc., P2E.1, 2008.

Hendricks, E. A., Montgomery, M. T., and Davis, C. A.: The role of "vortical" hot towers in the formation of tropical cyclone Diana (1984), J. Atmos. Sci., 61, 1209–1232, 2004.

Hildebrand, P. H., Lee, W.-C., Walther, C. A., Frush, C., Randall, M., Loew, E., Neitzel, R., Parsons, R., Testud, J., Baudin, F., and LeCornec, A.: The ELDORA/ASTRAIA airborne Doppler weather radar: High-resolution observations from TOGA COARE, Bull. Amer. Meteor. Soc., 77, 213–232, 1996.

Hock, T. F. and Franklin, J.L.: The NCAR GPS Dropwindsonde, Bull. Amer. Meteor. Soc., 80, 407–420, 1999.

Holton, J. R.: An Introduction to Dynamic Meteorology, Fourth ed. Academic Press, 535 pp, 2004.

Houze, R. A., Jr., Lee, W.-C., and Bell, M. M.: Convective contribution to the genesis of Hurricane Ophelia (2005), Mon. Wea. Rev., 137, 2778–2800, 2009.

Kepert, J.: The dynamics of boundary layer jets within the tropical cyclone core. Part I: Linear theory, J. Atmos. Sci., 58, 2469–2484, 2001.

Kepert, J. and Wang, Y.: The dynamics of boundary layer jets within the tropical cyclone core. Part II: Nonlinear enhancement, J. Atmos. Sci., 58, 2485–2501, 2001.

Marks, F. D., Jr. and Houze, R. A., Jr.: Airborne Doppler radar observations in Hurricane Debby, Bull. Amer. Meteor. Soc., 65, 569–582, 1984.

Montgomery, M. T., Nicholls, M. E., Cram, T. A., and Saunders, A. B.: A vortical hot tower route to tropical cyclogenesis, J. Atmos. Sci., 63, 355–386, 2006a.

Montgomery, M. T., Bell, M. M., Aberson, S. D., and Black, M. L.: Hurricane Isabel (2003): New insights into the physics of intense storms. Part I: Mean vortex structure and maximum intensity estimates, Bull. Amer. Meteor. Soc., 87, 1335, 2006b.

Nguyen, S. V., Smith, R. K., and Montgomery, M. T.: Tropical cyclone intensification and predictability in three dimensions, Q. J. R. Meteorol. Soc., 134, 563–582, 2008.

Ooyama, K. V.: Numerical simulation of the life cycle of tropical cyclones, J. Atmos. Sci., 26, 3–40, 1969.

Parsons, D., Harr, P. A., Nakazawa, T., Jones, S., and Weissmann, M.: An overview of the THORPEX-PACIFIC Asian regional campaign (T-PARC) during August-September 2008, Extended Abstracts, 28th Conf. on Hurricanes and Tropical Meteorology, Orlando, FL, Amer. Meteor. Soc., 7C.7, 2008.

Powell, M. D., Vickery, P. J., and Reinhold, T. A.: Reduced drag coefficient for high wind speeds in tropical cyclones, Nature, 422, 279–283, 2003.

Raymond, D. J., and Lopez-Carrillo, C.: The vorticity budget of developing Typhoon Nuri (2008), Atmos. Chem. Phys., 11, 147–163, 2011.

Reasor, P. D., Montgomery, M. T., and Bosart, L. F.: Mesoscale observations of the genesis of Hurricane Dolly (1996), J. Atmos. Sci., 62, 3151–3171, 2005.

Reasor, P. D., Eastin, M. D., and Gamache, J. F.: Rapidly intensifying Hurricane Guillermo (1997). Part I: Low-wavenumber structure and evolution, Mon. Wea. Rev., 137, 603–631, 2009.

Rogers, R. F., Aberson, S. D., Black, M. L., Black, P. G., Cione, J., Dodge, P., Dunion, J., Gamache, J. F., Kaplan, J., Powell, M. D., Shay, N., Surgi, N., and Uhlhorn, E. W.: The intensity forecasting experiment: A NOAA multiyear field program for improving tropical cyclone intensity forecasts, Bull. Amer. Meteor. Soc., 87, 1523–1537, 2006.

Sanger, N. T.: Mission report for Tropical Storm Jangmi from 24 - 25 Sep 2008, http://catalog.eol.ucar.edu/cgi-bin/tparc_2008/htmlwrap?file_url=/tparc_2008/report/usaf_c130/20080924/report.usaf_c130.200809241713.mission_summary.html, 2008a.

Sanger, N. T.: Mission report for Supertyphoon Jangmi from 27 Sep 2008, http://catalog.eol.ucar.edu/cgi-

bin/tparc_2008/htmlwrap?file_url=/tparc_2008/report/usaf_c130/20080927/report.usaf_c130.200809270208.mission_summary.html, 2008b.

Sanger, N. T.: An observational study of tropical cyclone spin-up in Supertyphoon Jangmi and Hurricane Georges, Ph.D dissertation, Dept. of Meteorology, Naval Postgraduate School, 187 pp., 2011.

Shin, S. and Smith, R. K.: Tropical cyclone intensification and predictability in a minimal three dimensional model, Q. J. R. Meteorol. Soc., 134, 1661–1671, 2008.

Smith, R. K. and Montgomery, M. T.: Hurricane boundary-layer theory, Q. J. R. Meteorol. Soc., 136, 1665–1670, 2010.

Smith, R. K., Montgomery, M. T., and Vogl, S.: A critique of Emanuel's hurricane model and potential intensity theory, Q. J. R. Meteorol. Soc., 134, 551–561, 2008.

Smith, R. K., Montgomery, M. T., and Nguyen, S. V.: Tropical cyclone spin up revisited, Q. J. R. Meteorol. Soc., 135, 1321–1335, 2009.

Smith R. K. and Thomsen, G. L.: Dependence of tropical-cyclone intensification on the boundary layer representation in a numerical model, Q. J. R. Meteorol. Soc., 136, 1671-1685, 2010.

Testud, J., Hildebrand, P. H., and Lee, W.-C.: A procedure to correct airborne Doppler radar data for navigation errors using the echo returned from the Earth's surface, J. Atmos. Oceanic Technol., 12, 800–820, 1995.

Uhlhorn, E. W., Black, P. G., Franklin, J. L., Goodberlet, M., Carswell, J., and Goldstein, A. S.: Hurricane surface wind measurements from an operational stepped frequency microwave radiometer, Mon. Wea. Rev., 135, 3070–3085, 2007.

Williamson, S. P.: Office of federal coordinator for meteorological services and supporting research (OFCM) national hurricane operations plan, FCM-P12-2009, 160 pp., 2009.

Willoughby, H. E.: Gradient balance in tropical cyclones, J. Atmos. Sci., 47, 265-274, 1990.

Willoughby, H. E. and Chelmow, M. B.: Objective determination of hurricane tracks from aircraft observations, Mon. Wea. Rev., 110, 1298–1305, 1982.

Wissmeier U. and Smith, R. K.: Tropical cyclone convection: The effects of ambient vertical vorticity, Q. J. R. Meteorol. Soc., 137, 845-857, 2011.

Zhang, D., Liu, Y., and Yau, M. K.: A multiscale numerical study of Hurricane Andrew (1992). Part IV: Unbalanced flows, Mon. Wea. Rev., 129, 92–107, 2001.

Zhang, J. A., Drennan, W. M., Black, P. G., and French, J. R.: Turbulence structure of the hurricane boundary layer between the outer rainbands, J. Atmos. Sci., 66, 2455–2467, 2009.

Zhang J. A., Rogers, R. F., Nolan, D. S., and Marks, F. D.: On the characteristic height scales of the hurricane boundary layer. Mon. Wea. Rev., 139, 2523-2535, 2011.

Table 1. Radius of maximum total surface wind speed (RMW) in six quadrants based on Stepped Frequency Microwave Radiometer (SFMR) observations listed in chronological order from the first radial leg to the last radial leg (East-Southeast-ESE, West-Southwest-WSW, South-Southeast-SSE, Northeast-NE, Northwest-NW, and Southeast-SE) for TS Jangmi from 1856 UTC 24 Sep 08 to 0047 UTC 25 Sep 08. The SFMR data was collected along three WC-130J radial legs that were flown while penetrating the storm center. Due to storm asymmetry, a third-degree polynomial curve fit of the observations was used to identify the RMW in each quadrant.

QUADRANT	TIME	SFMR RMW	FL RMW
ESE	1856-1947 UTC 24 Sep	75 Km	125 Km
WSW	1947-2022 UTC 24 Sep	70 Km	125 Km
SSE	2114-2147 UTC 24 Sep	90 Km	90 Km
NE	2147-2257 UTC 24 Sep	65 Km	100 Km
NW	2258-2352 UTC 24 Sep	85 Km	120 Km
SE	0000-0047 UTC 25 Sep	65 Km	70 Km

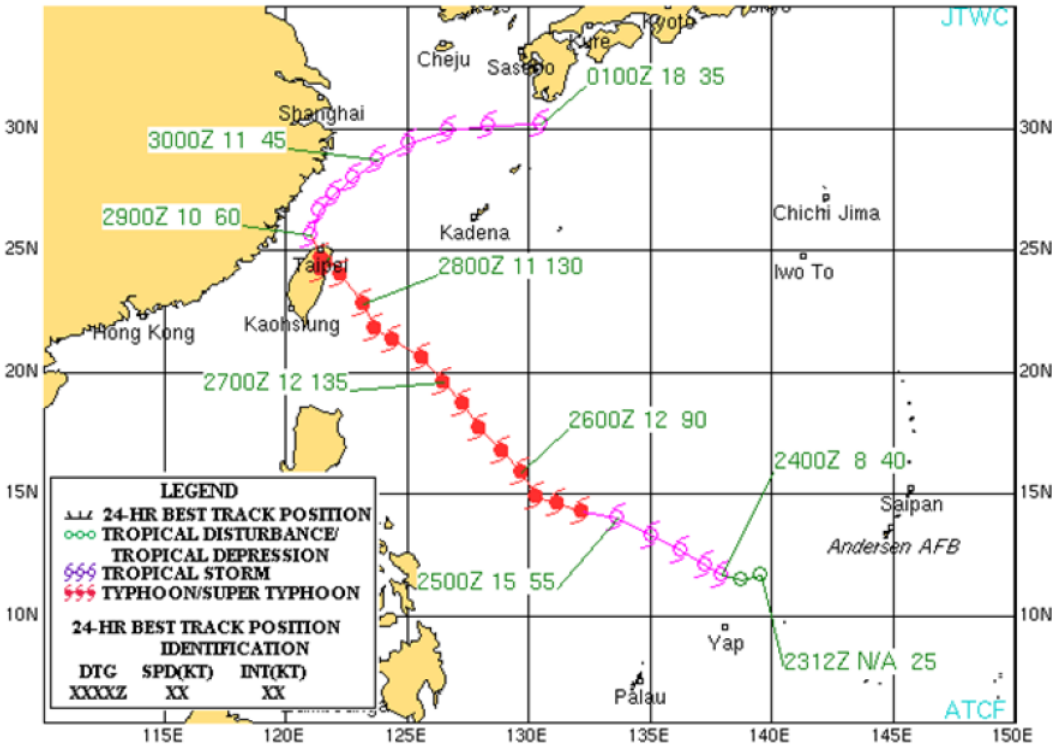

Figure 1. JTWC best-track of Supertyphoon Jangmi from Cooper and Falvey (2009). Green circle indicates tropical depression, open purple tropical cyclone symbol is tropical storm, and closed red tropical cyclone symbol is typhoon. Text indicates date-time group (DDHH), storm speed (kt), and storm intensity (kt).

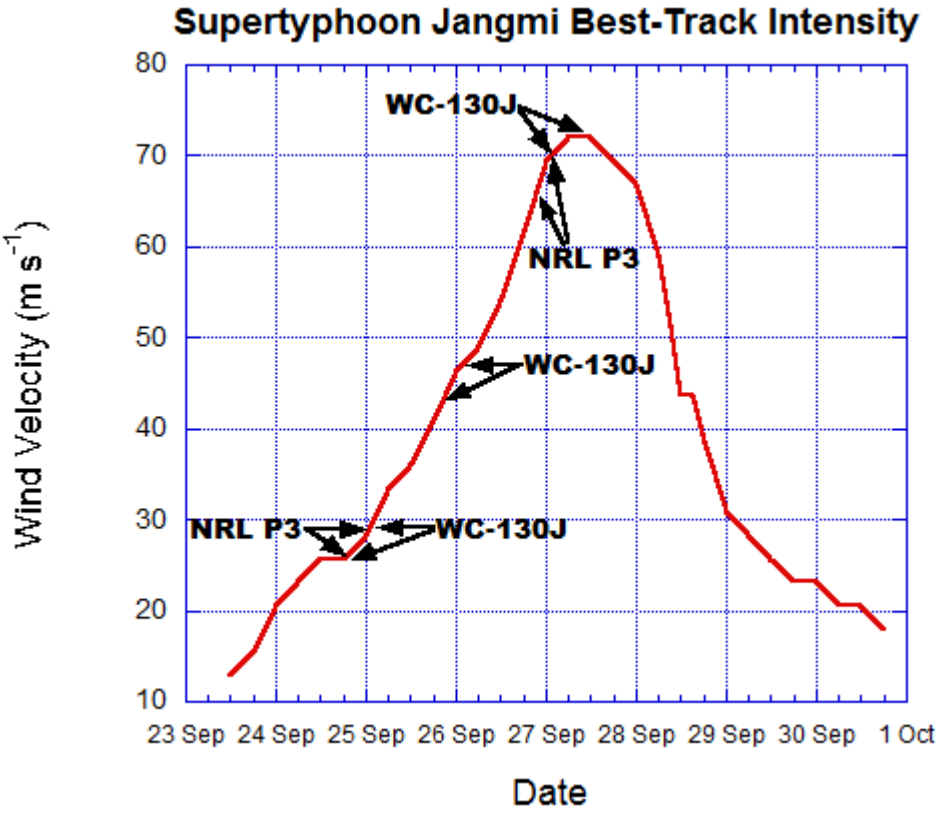

Figure 2. JTWC best-track intensity (m s^{-1}) for Supertyphoon Jangmi from 23 September to 30 Sep 2008. Arrows indicate start and stop times of the various research missions within the storm environment.

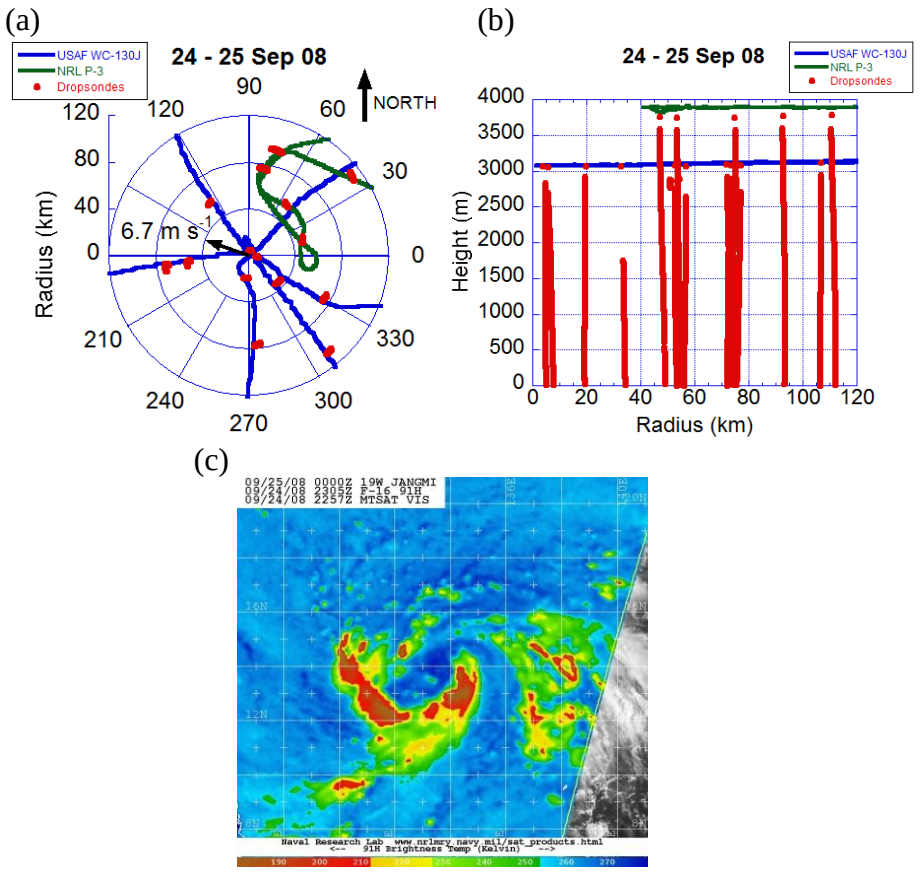

Figure 3. Dropsonde locations, trajectories, and aircraft flight tracks in TS Jangmi from 1927 UTC 24 Sep 08 – 0019 UTC 25 Sep 08. Storm-relative data distributions in geographical (a) radius-azimuth (*R*-θ) coordinates and (b) radius-height (*R*-*Z*) coordinates. The plots display the WC-130J track (blue), the NRL P-3 track (green), and dropsonde trajectories (red). Dropsondes move cyclonically in (a). The thin black arrow in the center of (a) is the storm motion vector, with storm translation speed indicated in light black text (m s^{-1}). Microwave satellite imagery at (c) 2305 UTC 24 Sep shown to provide context of storm structure during this stage.

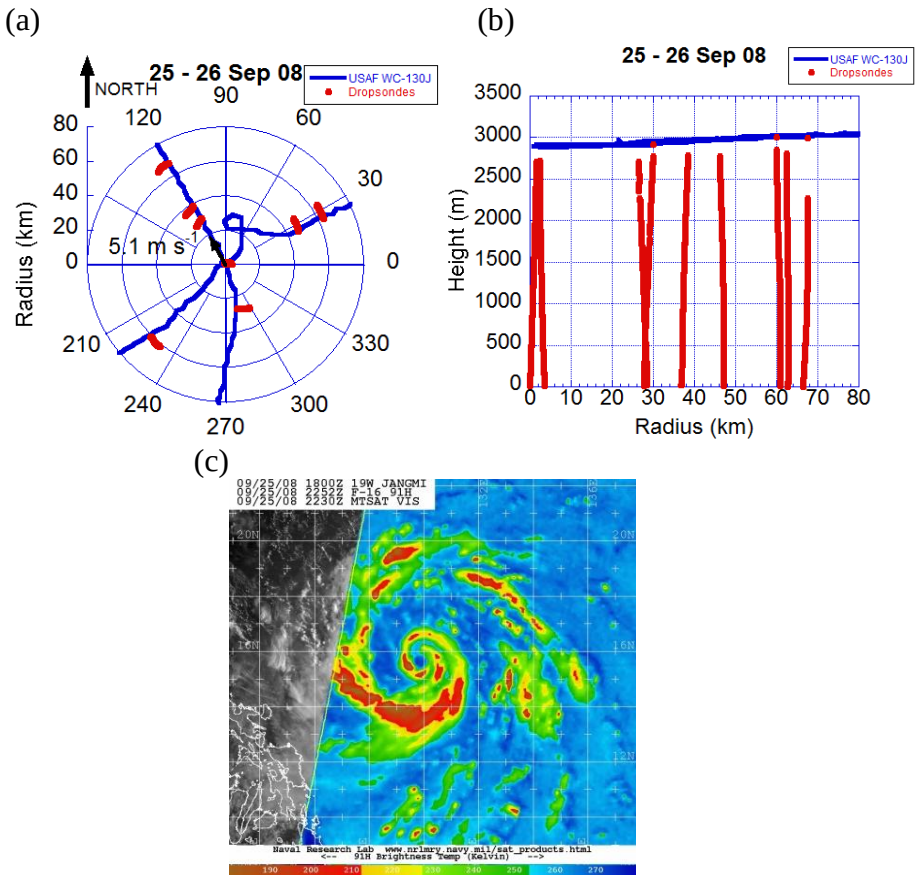

Figure 4. Dropsonde locations, trajectories, and aircraft flight tracks in Typhoon Jangmi from 2333 UTC 25 Sep 08 – 0113 UTC 26 Sep 08. Storm-relative data distributions in geographical (a) radius-azimuth (*R*-θ) coordinates and (b) radius-height (*R*-*Z*) coordinates. The plots display the WC-130J track (blue) and dropsonde trajectories (red). Dropsondes move cyclonically in (a). The thin black arrow in the center of (a) is the storm motion vector, with storm translation speed indicated in light black text (m s^{-1}). Microwave satellite imagery at (c) 2252 UTC 25 Sep shown to provide context of storm structure during this stage.

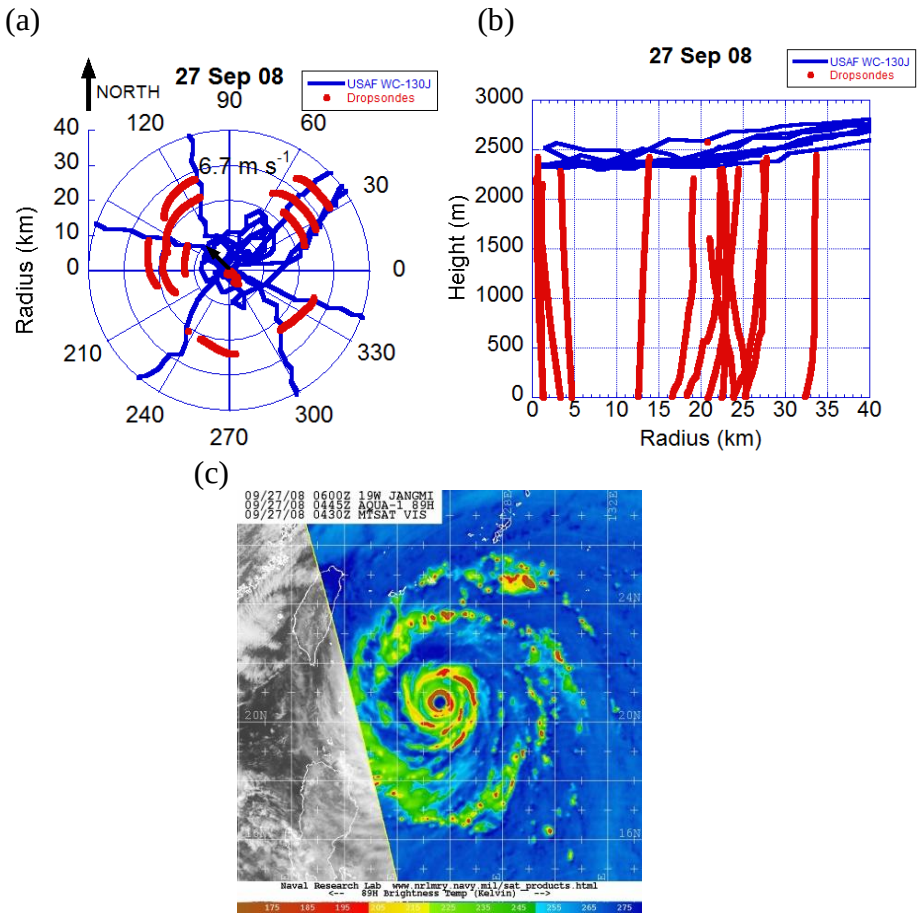

Figure 5. Dropsonde locations, trajectories, and aircraft flight tracks in Supertyphoon Jangmi from 0615 – 0957 UTC 27 Sep 2008. Storm-relative data distributions in geographical (a) radius-azimuth (R-θ) coordinates and (b) radius-height (R-Z) coordinates. The plots display the WC-130J track (blue) and dropsonde trajectories (red). Dropsondes move cyclonically in (a). The thin black arrow in the center of (a) is thoe storm motion vector, with storm translation speed indicated in light black text (m s^{-1}). Microwave satellite imagery at (c) 0445 UTC 27 Sep shown to provide context of storm structure during this stage.

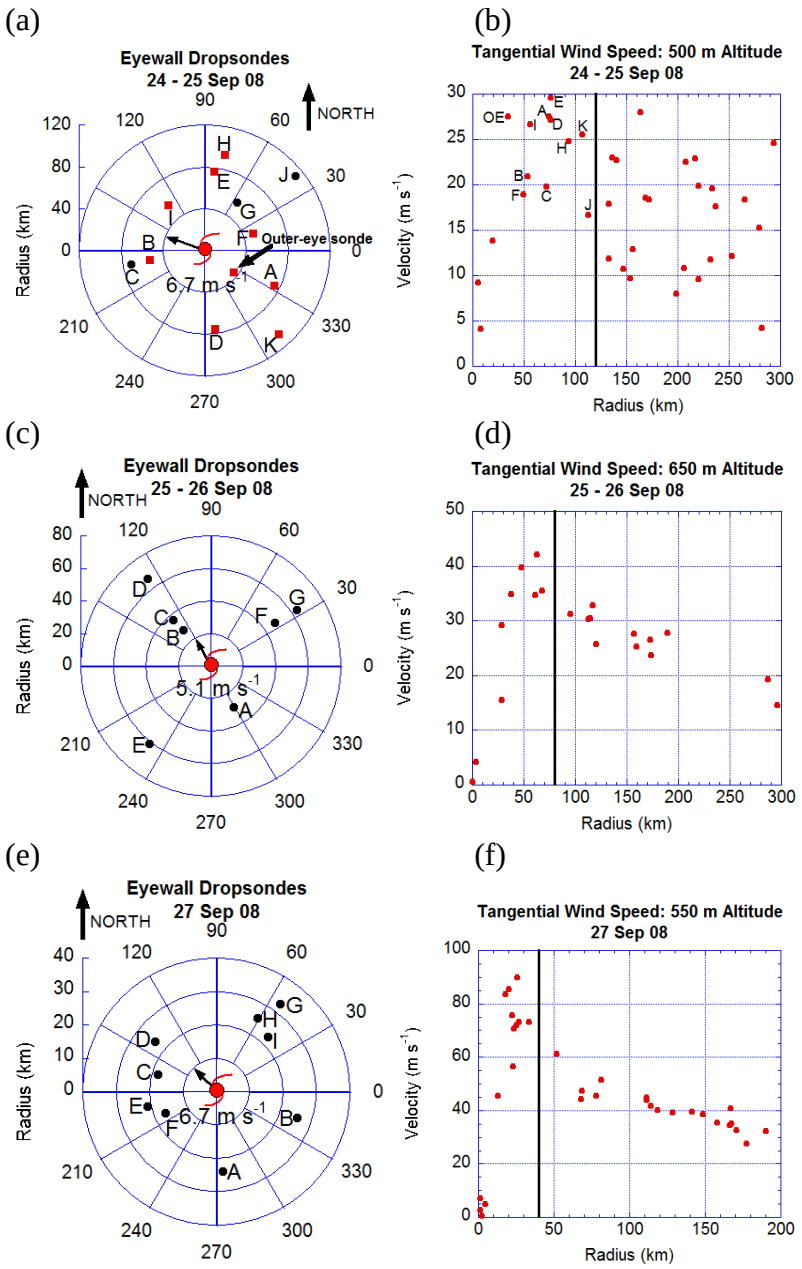

Figure 6. (a) Near-surface radius versus azimuth displays of *only eyewall dropsondes* in geographic-oriented coordinates; dropsondes listed in order (A-K) for (a) TS Jangmi, (c) TY Jangmi, and (e) STY Jangmi. (b) Storm-relative tangential wind (m s^{-1}) from dropsonde observations versus radius out to 300 km radius at an altitude of ~ 500 m for TS Jangmi (red dots), (d) same as (b) but at ~ 650 m altitude out to 300 km for TY Jangmi, and (f) same as (b) but at ~ 550 m altitude out to 200 km for STY Jangmi. Thin, black arrow

depicts storm motion vector with storm translation speed indicated in light black text near the storm translation vector (in m s^{-1}). Vertical black line delineates the start of the inner-core region of the storm. Red squares in (a) show significant supergradient tangential winds during tropical storm stage shown later in Figure 11b.

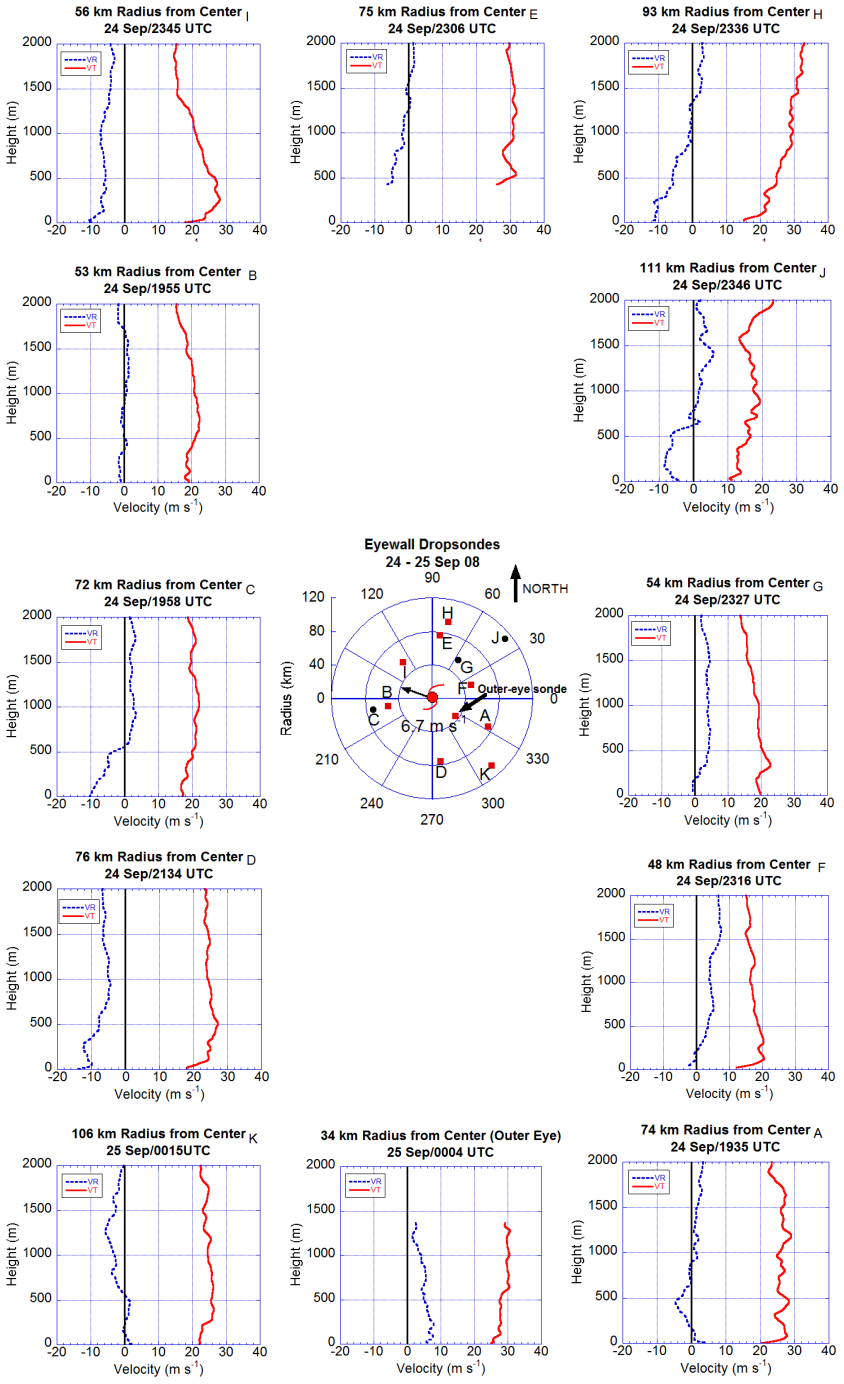

Figure 7. TS Jangmi tangential wind (solid red line) and radial wind (dotted blue line) profiles in m s^{-1} for eyewall sondes from 24 – 25 Sep 2008. Dropsonde locations shown in geographic-oriented R-θ plot in middle labeled with letters (A - K) according to order of launch placed relative to the storm center.

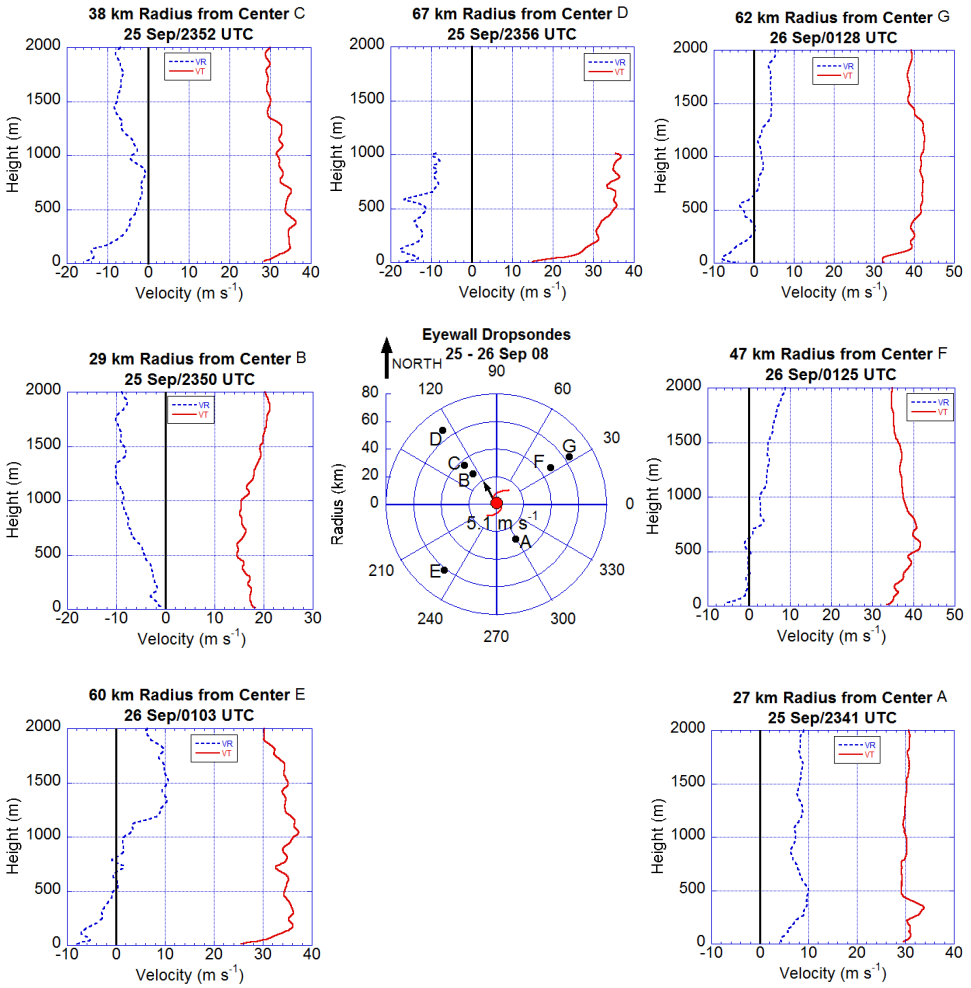

Figure 8. Typhoon Jangmi tangential wind (solid red line) and radial wind (dotted blue line) profiles in units of m s^{-1} for all eyewall dropwindsondes from 25 – 26 Sep 2008. Dropsonde locations shown in geographic-oriented *R*-θ plot in middle of page are labeled with letters (A - G) according to order of launch and placed in approximate location relative to the storm center. The dropsonde altitudes are all at or near the surface.

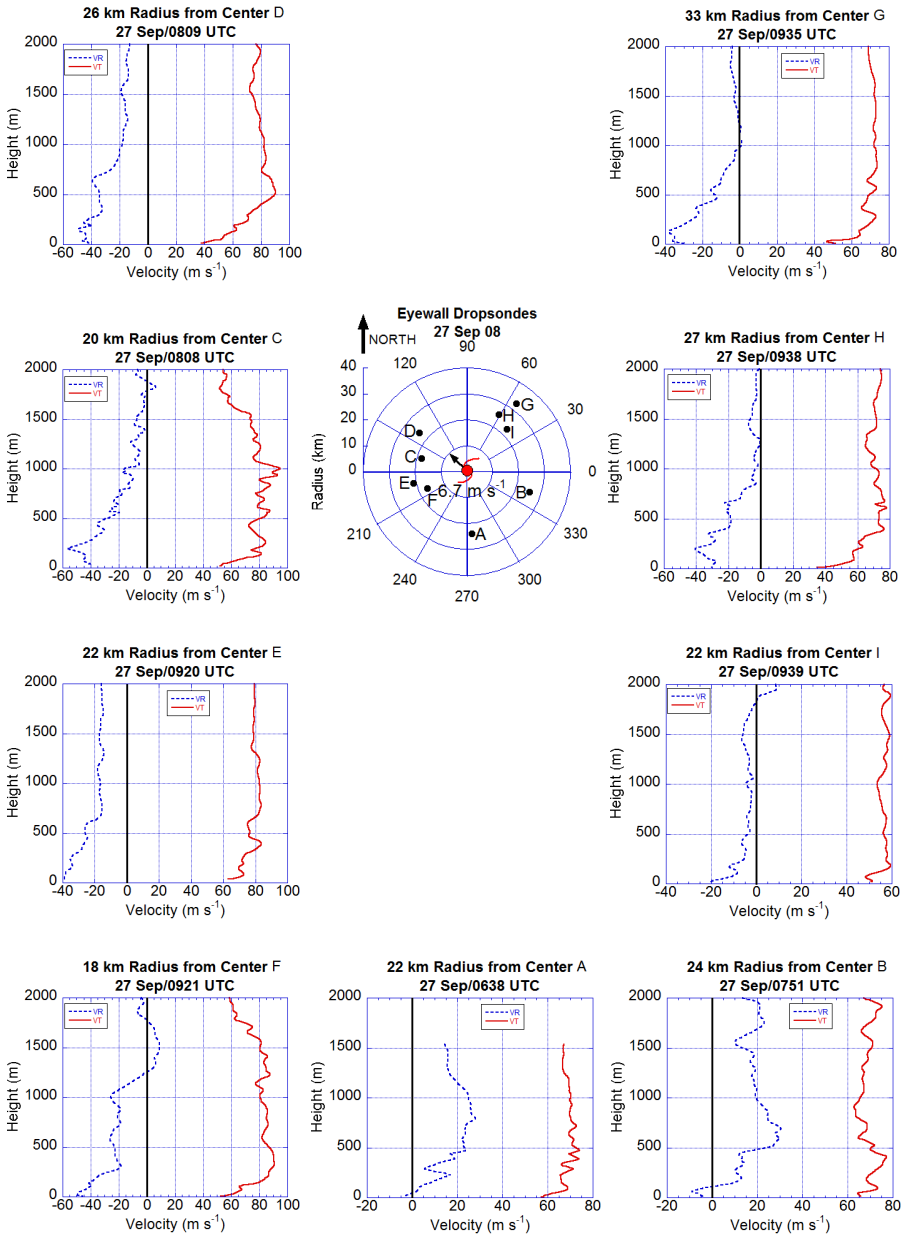

Figure 9. Supertyphoon Jangmi tangential wind (solid red line) and radial wind (dotted blue line) profiles in m s^{-1} for all eyewall dropwindsondes on 27 September 2008. Dropsonde locations shown in geographic-oriented *R*-θ plot in middle of page are labeled with letters (A - I) according to order of launch and placed in approximate location relative to the storm center. The dropsonde altitudes are all at or near the surface.

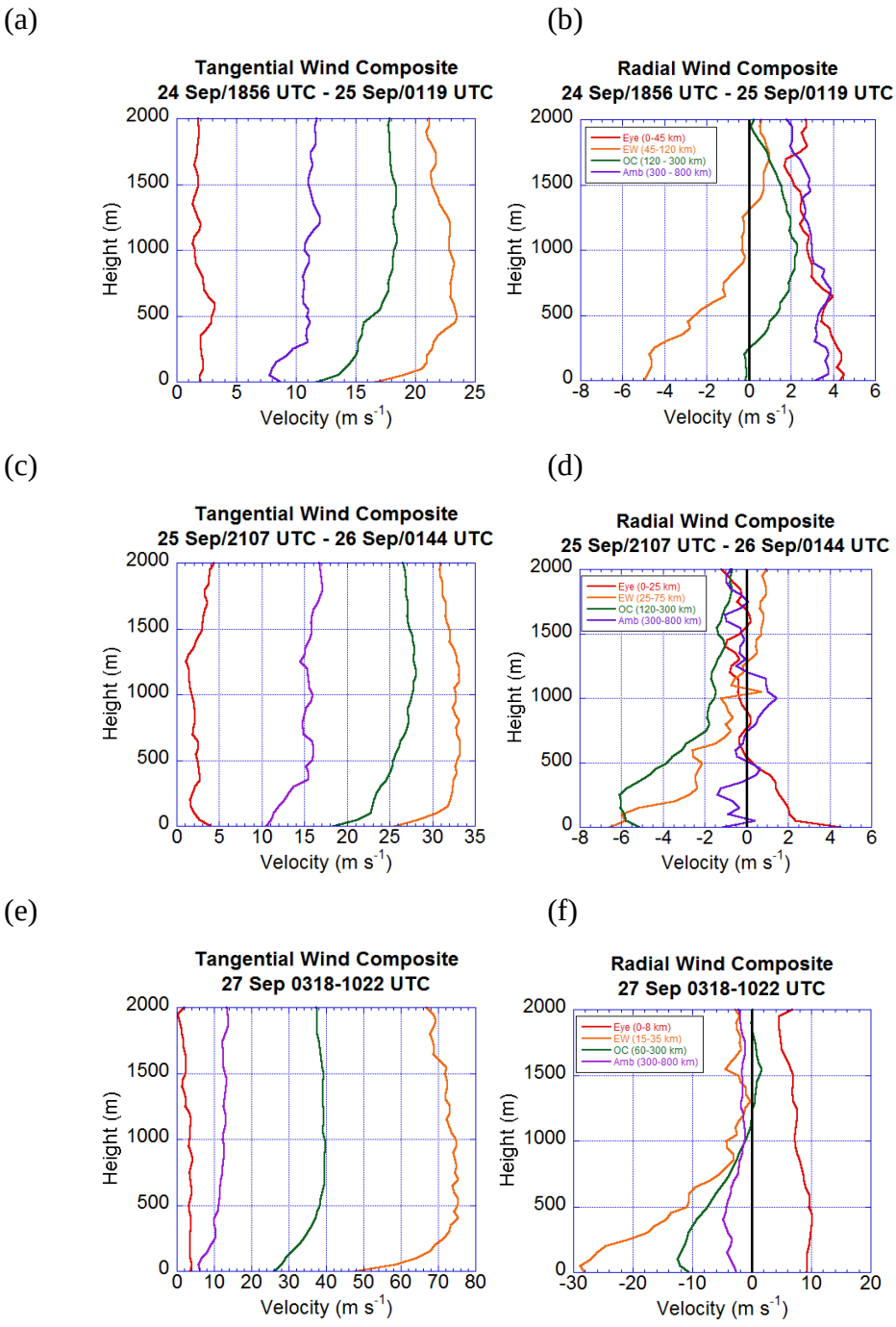

Figure 10. Low-level (0 - 2 km) tangential wind speed (m s^{-1}) in left column and radial wind speed (m s^{-1}) in right column composite soundings for (a,b) TS Jangmi, (c,d) TY Jangmi, and (e,f) STY Jangmi in the eye (red line), eyewall (EW; orange line), outer core (OC; green line), and ambient (Amb; purple line) regions of storm.

(a) (b)

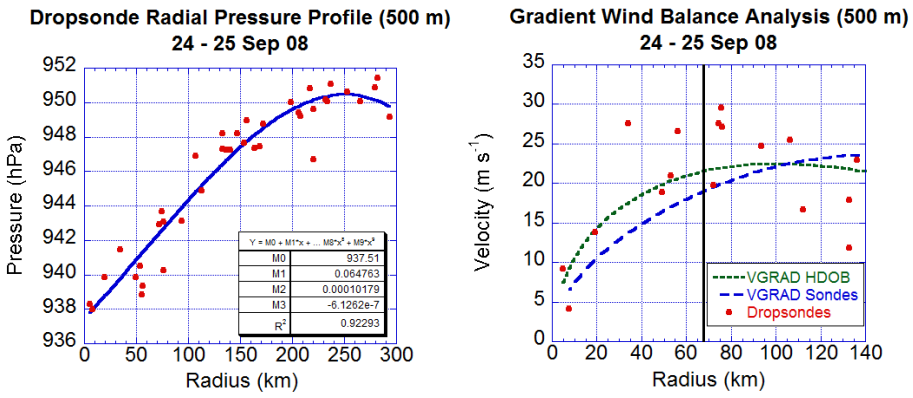

(c) (d)

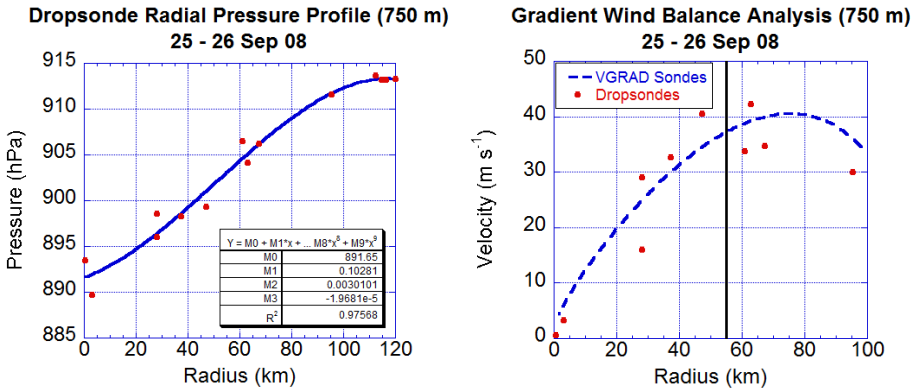

(e) (f)

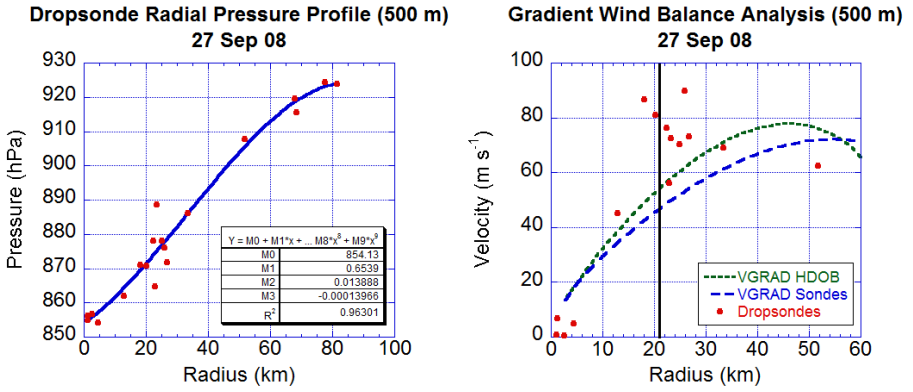

Figure 11. Observed pressure (hPa) from dropsondes (solid red circles) and 3rd degree polynomial fit (solid blue line) at (a) 500 m for TS Jangmi, (c) 750 m for Typhoon Jangmi, and (e) 500 m for Supertyphoon Jangmi. Table shows curve fit coefficients and r^2 values. Tangential wind in m s^{-1} at (b) 500 m for TS Jangmi (d) 750 m for Typhoon Jangmi, and (f) 500 m for Supertyphoon Jangmi from dropsondes (solid red circles) and gradient wind

from HDOB data (short-dashed green curve) and dropsonde data (long-dashed blue line). The solid black vertical lines in (a-d) denote the mean RMW.

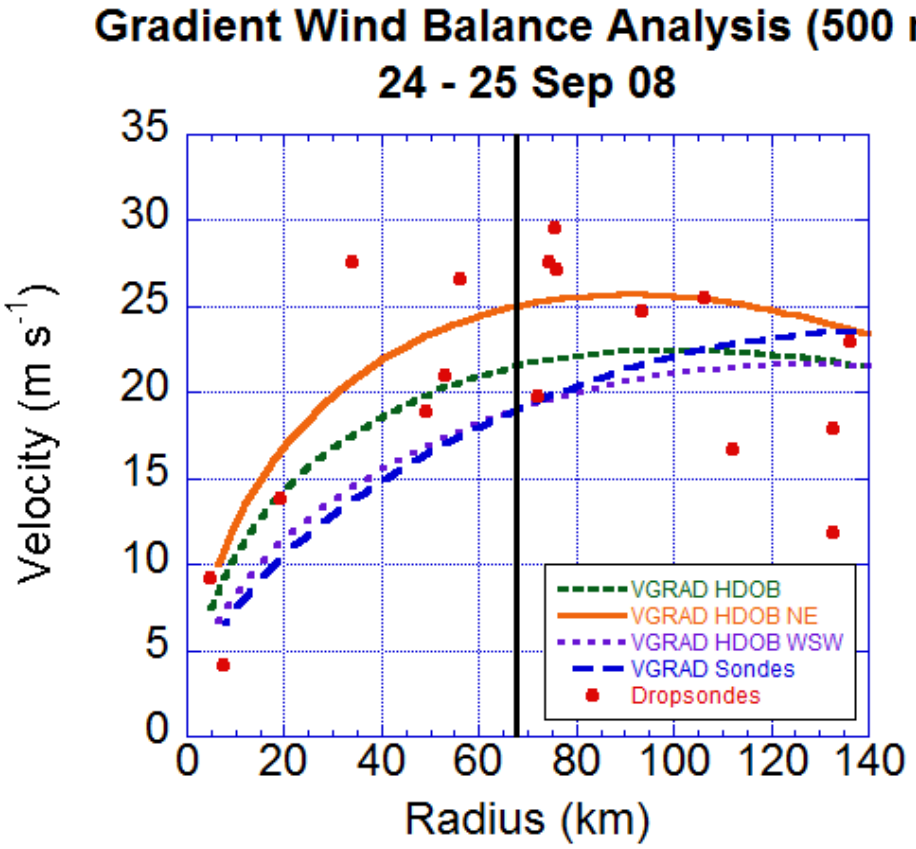

Figure 12. Tangential wind speed in m s^{-1} at 500 m altitude for TS Jangmi from dropsondes (solid red circles) and gradient wind speed in m s^{-1} derived from all flight-level HDOB data (short-dashed green curve), flight-level HDOB data in NE Quadrant (solid orange line), flight-level HDOB data in WSW Quadrant (dotted purple line), and dropsonde data (long-dashed blue line). The solid black vertical line denotes the axisymmetric RMW based on the SFMR data. The NE and WSW Quadrant curves were used to plot an upper and lower bound of the gradient wind curve, respectively. The NE Quadrant contained the steepest pressure gradient, while the WSW Quadrant had the flattest pressure gradient.

(a)

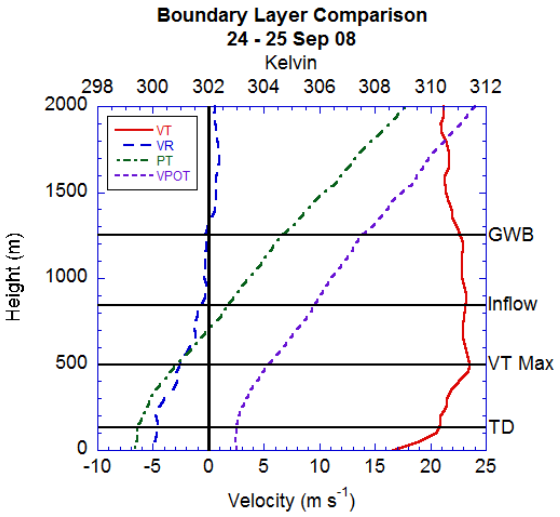

(b)

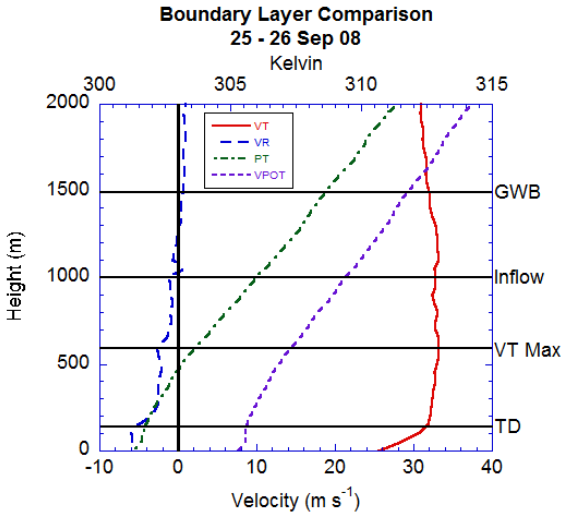

(c)

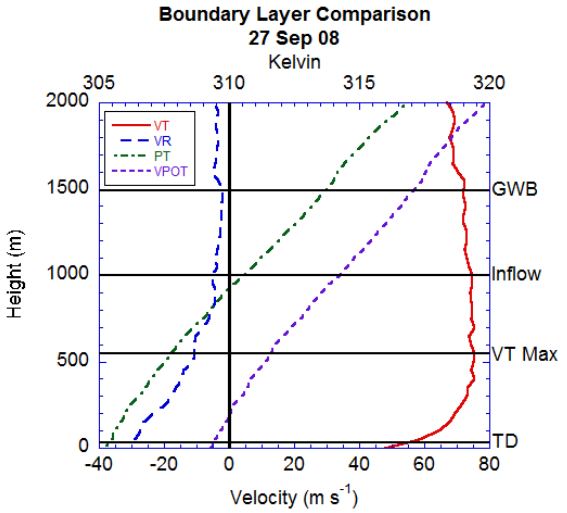

Figure 13. Boundary-layer height comparison for (a) TS Jangmi, (b) TY Jangmi, and (c) STY Jangmi using thermodynamic and dynamic definitions. Dynamic boundary layer (layer of significant gradient wind imbalance) depth depicted by solid horizontal black line labeled "GWB"; layer of significant radial inflow (≥ 20% of near-surface value) shown by solid horizontal black line marked "Inflow"; thermodynamic boundary layer (well-mixed) displayed with solid horizontal black line labeled "TD." The height of maximum tangential wind speed depicted with solid horizontal black line labeled "VT Max." Tangential wind speed composite (solid red line), radial wind speed composite (dashed blue line), potential temperature composite (dotted-dashed green line), and virtual potential temperature (small dashed purple line) are plotted on graph.

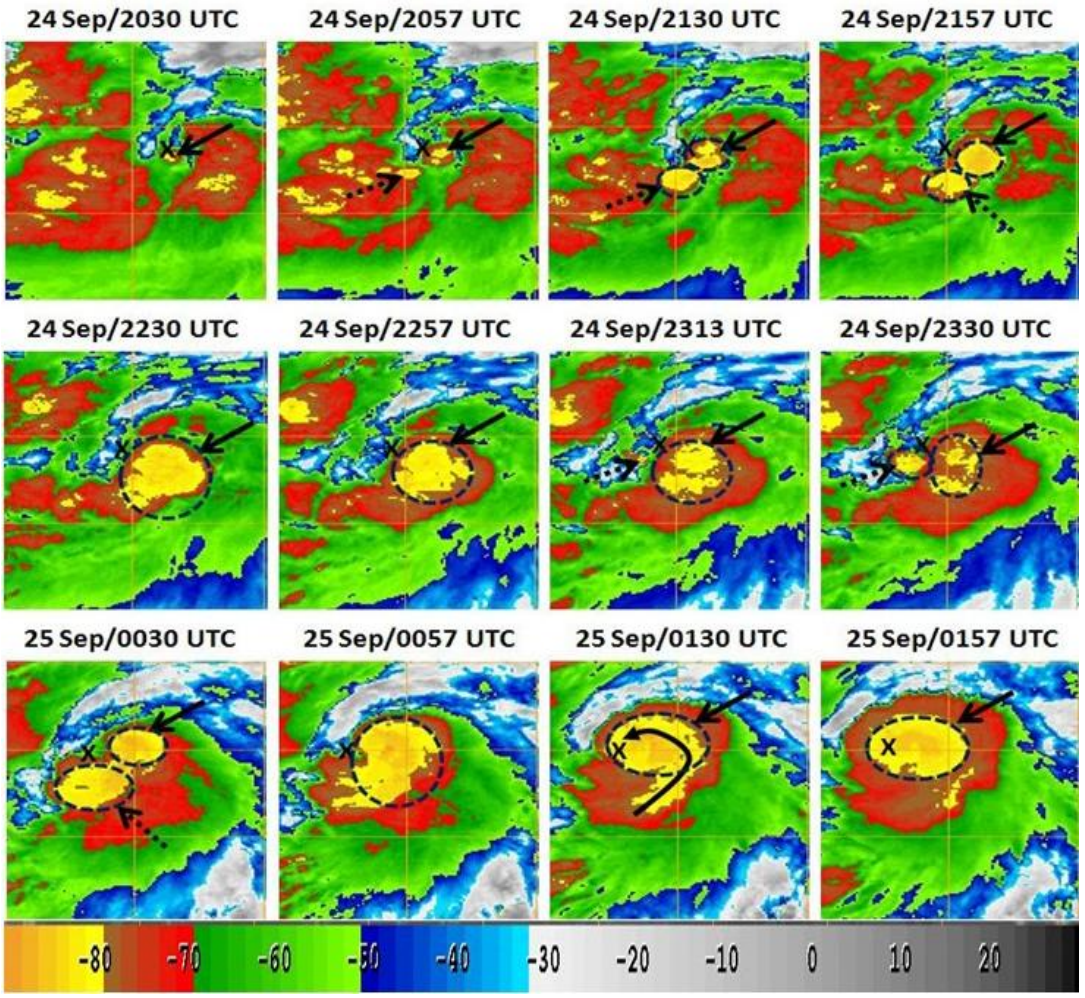

Figure 14. Series of 1-km MTSAT infrared imagery of deep convective clouds in TS Jangmi from 2030 UTC 24 September – 0157 UTC 25 September 2008. Dashed black circles indicate deep convection and its approximate areal extent and shape. TS Jangmi center based on the 10-minute storm track file (see Chapter III, Section E for description) is shown with black "**X**." Note the increase in horizontal coverage in both areas of deep convective clouds, possible cloud merger in 0057 UTC 25 Sep panel, and inward spiral of clouds in second to last panel at 0130 UTC 25 Sep. The color bar at bottom of plot associates cloud-top temperatures with various colors. The low est cloud-top temperatures are shown with shades of red and yellow (-70°C to -90°C). Imagery courtesy of Naval Research Laboratory, Monterey, CA.

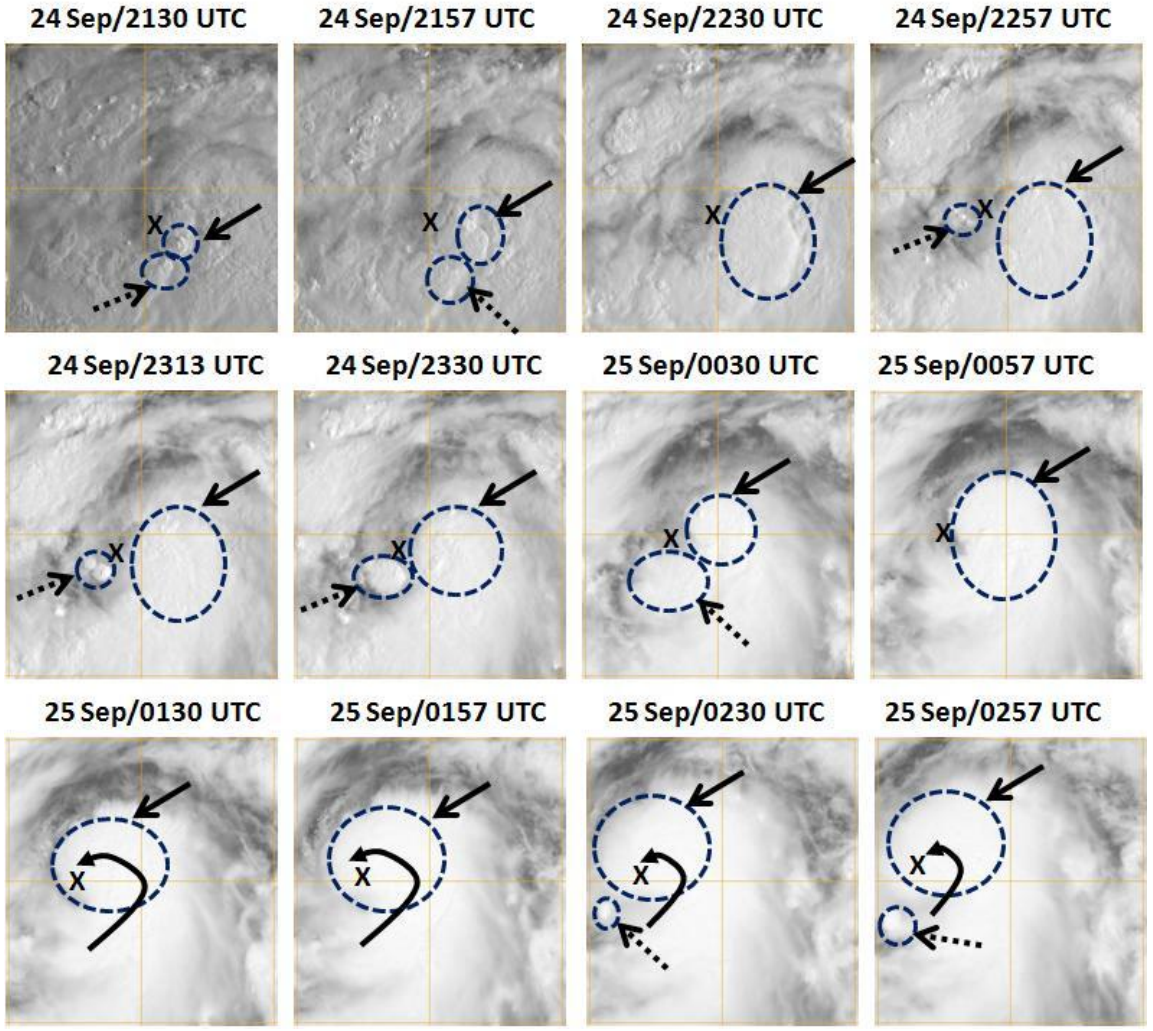

Figure 15. Series of 1-km MTSAT visible imagery depicting deep convective clouds in TS Jangmi from 2130 UTC 24 September – 0257 UTC 25 September 2008. Dashed blue circles indicate areas of deep convection and its approximate areal extent, shape, and overshooting tops. TS Jangmi center based on the 10-minute storm track file is shown with black "X." Note the increase in horizontal coverage of deep convective clouds, possible cloud merger in 0057 UTC 25 Sep panel, and inward spiral of clouds in the last four panels (0130 – 0257 UTC 25 Sep). Imagery courtesy of Naval Research Laboratory, Monterey, CA.

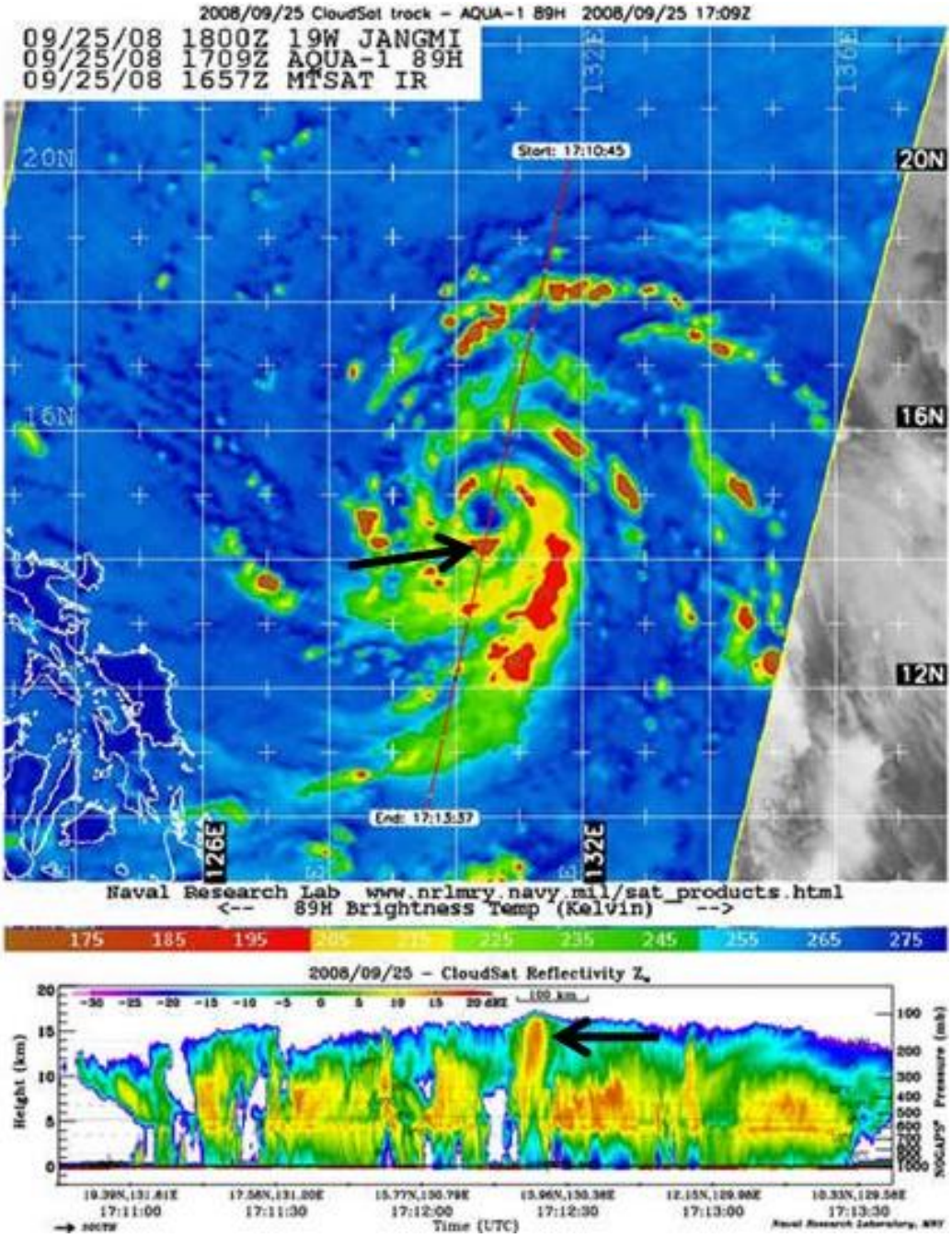

Figure 16. CLOUDSAT reflectivity (bottom) through Typhoon Jangmi during pass from north to south from 1711 – 1713 UTC 25 September 2008 with associated AQUA microwave satellite image at 1709 UTC 25 September 2008 (top). Note the deep convection in the southern eyewall extending up to 17 km altitude. The color bar in between the reflectivity and satellite image associates cloud-top temperatures in Degrees Kelvin (K) with various colors. The lowest cloud-top temperatures are shown with shades of red and orange (200K to

170K). Images courtesy of Colorado State University/NESDIS/CIRA, Fort Collins, CO.

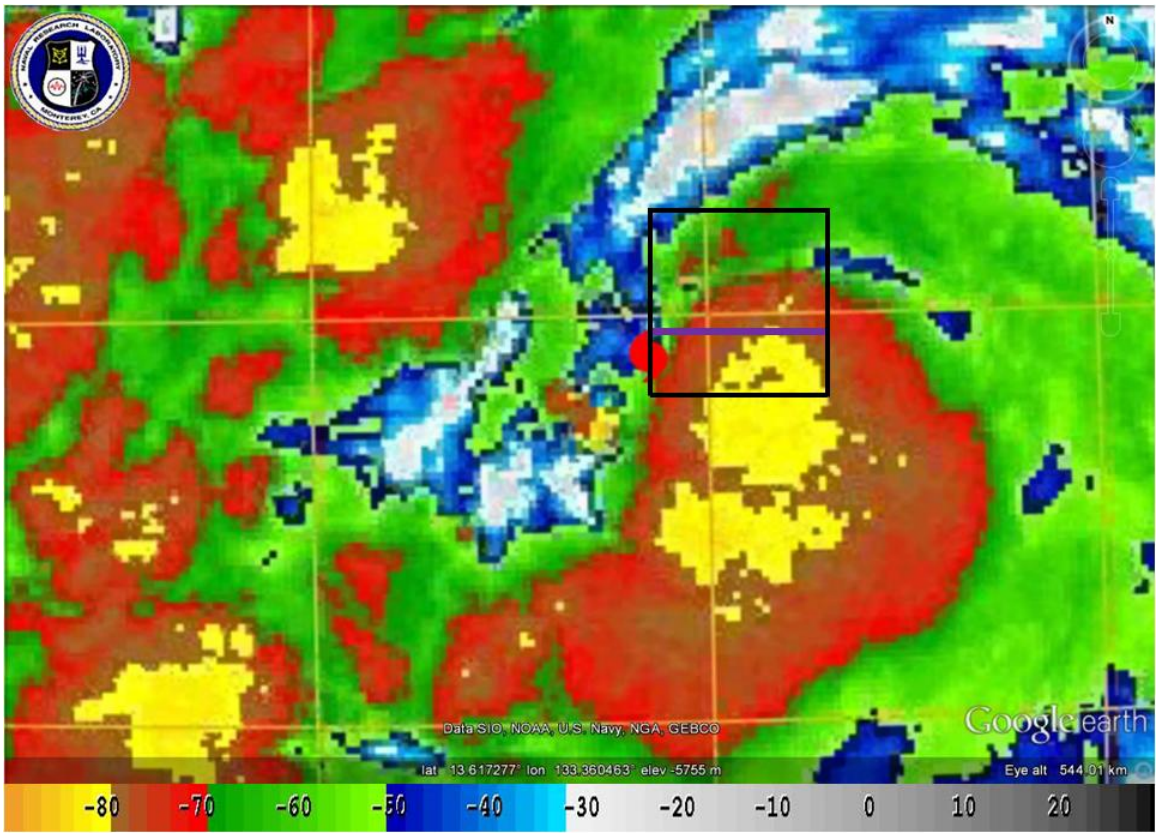

Figure 17. 1 km MTSAT infrared imagery at 2313 UTC 24 September 2008 during NRL P-3 ELDORA mission into Tropical Storm Jangmi. The 0000 UTC 25 Sep storm position based on the 10-minute storm track file is shown with red tropical cyclone symbol. The ELDORA data domain is shown with the black rectangle. The location of the cross-section shown later in Figure 20 is depicted by the solid purple line. The color bar at the bottom of the image associates cloud-top temperatures with various colors. The lowest cloud-top temperatures are shown with shades of red and yellow (-70°C to -90°C).

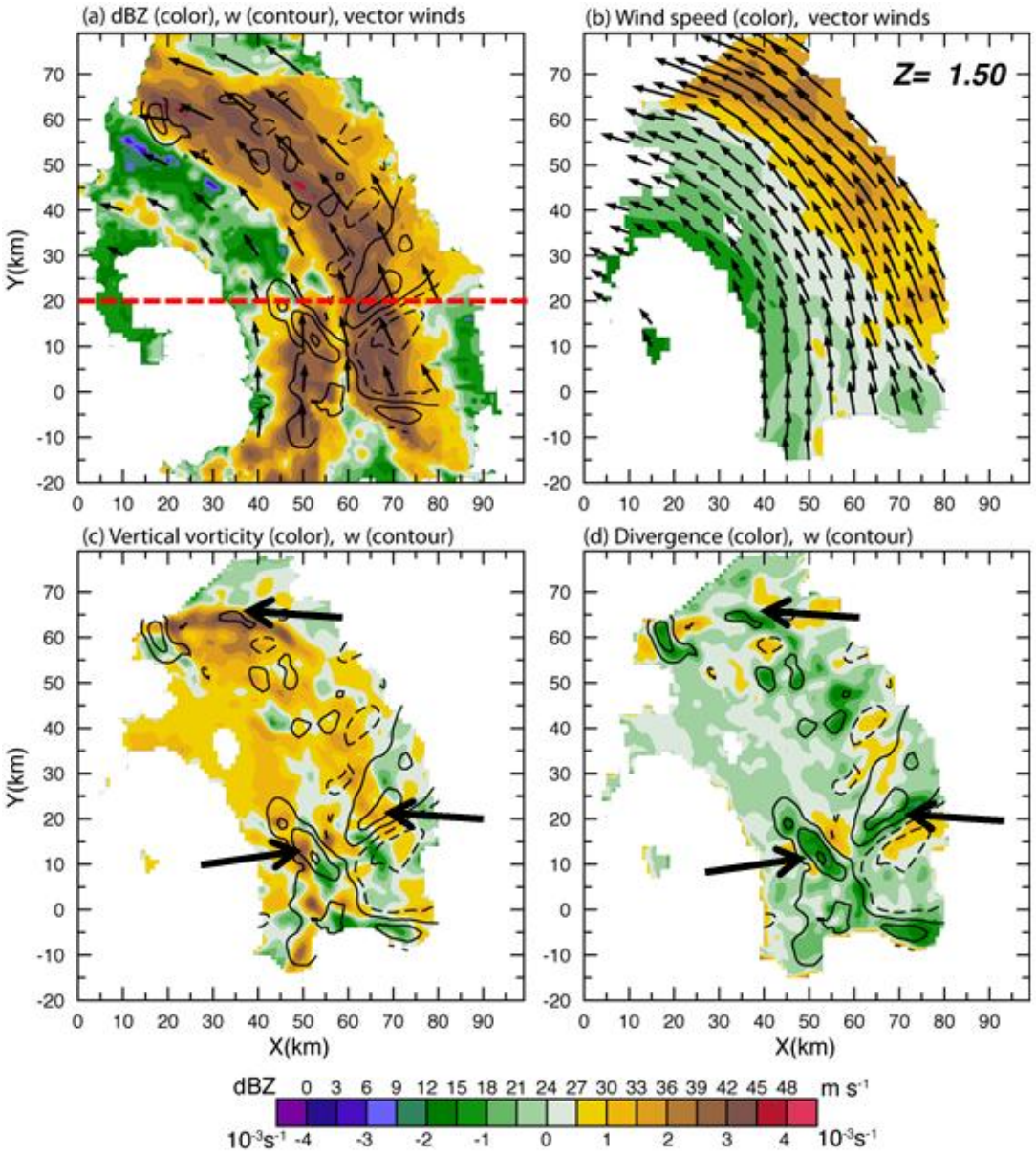

Figure 18. ELDORA analysis from 2310 -2320 UTC 24 September 2008. Panel (a) shows horizontal plan view of radar reflectivity (color, dBZ), wind vectors, and vertical velocity (contour, 2 m s^{-1} increments; solid contours are positive) at 1.5 km altitude. The red dashed line indicates location of the vertical slice to be examined later in Figure 20. Panel (b) depicts wind vectors and speed (color contoured in m s^{-1}) in the earth-relative frame at 1.5 km altitude. Panel (c) shows horizontal plan view of relative vertical vorticity (color, 10^{-3} s^{-1}) and vertical velocity (contour, 2 m s^{-1} increments; solid contours are positive) at 1.5 km altitude. Panel (d) shows divergence (color, 10^{-3} s^{-1}) and vertical velocity (contour, 2 m s^{-1} increments; solid

contours are positive) at 1.5 km altitude. Arrows show regions of cyclonic vorticity, convergence, and updrafts.

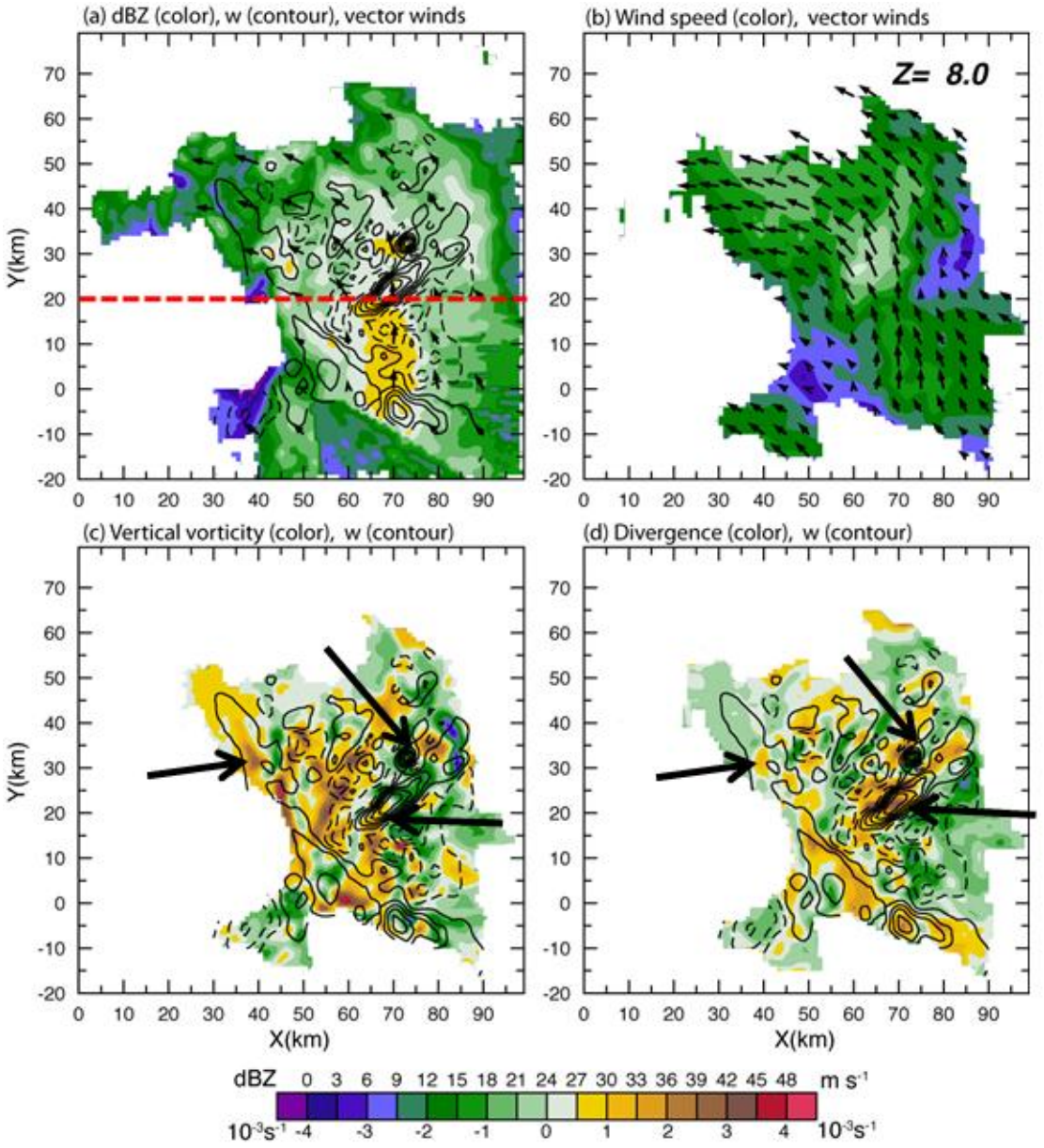

Figure 19. ELDORA analysis from 2310 -2320 UTC 24 September 2008. Panel (a) shows horizontal plan view of radar reflectivity (color, dBZ), wind vectors, and vertical velocity (contour, 2 m s^{-1} increments; solid contours are positive) at 8 km altitude. The red dashed line indicates location of the vertical slice to be examined later in Figure 20. Panel (b) depicts wind vectors and speed (color contoured in m s^{-1}) in the earth-relative frame at 8.0 km altitude. Panel (c) shows horizontal plan view of relative vertical vorticity (color, 10^{-3} s^{-1}) and vertical velocity (contour, 2 m s^{-1} increments; solid contours are positive) at 8.0 km altitude. Panel (d) shows divergence (color, 10^{-3} s^{-1}) and vertical velocity (contour, 2 m s^{-1} increments; solid

contours are positive) at 8 km altitude. Arrows show regions of cyclonic vorticity, divergence, and updrafts.

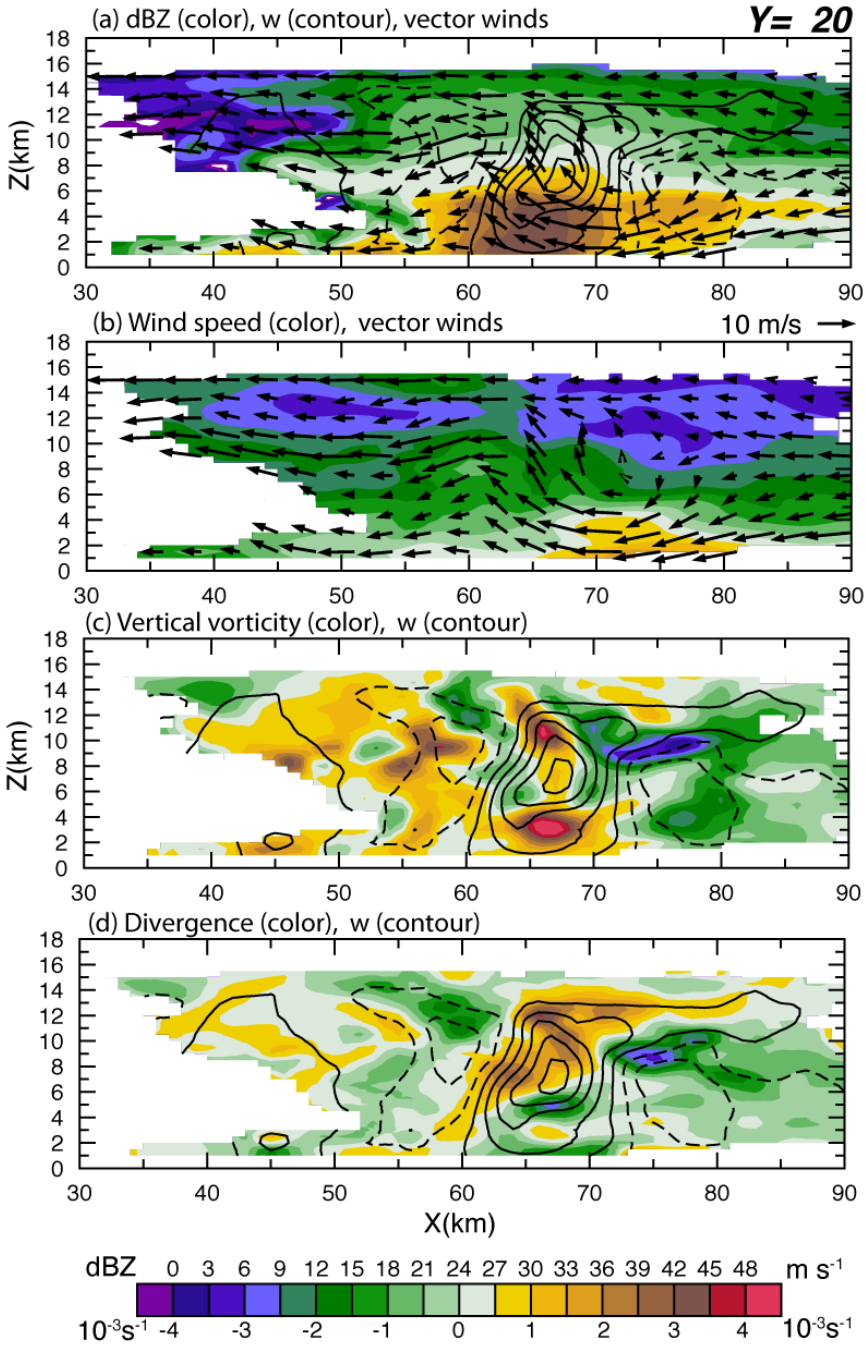

Figure 20. ELDORA vertical-zonal cross-section analysis from 2310-2320 UTC 24 September 2008. Panel (a) depicts reflectivity (color), wind vectors in the vertical-zonal plane, and vertical velocity (contours, 2 m s^{-1} increments; solid contours are positive). Panel (b) shows earth-relative wind velocity in m s^{-1} (color), and wind vectors in the X-Z plane. Panel (c) depicts vertical relative vorticity (color) and vertical velocity in m s^{-1}

(contours, 2 m s^{-1} increments; solid contours are positive). Panel (d) depicts divergence (color, 10^{-3} s^{-1}) and vertical velocity (contour, 2 m s^{-1} increments).